Available on CMS information server

CMS NOTE-2008/010

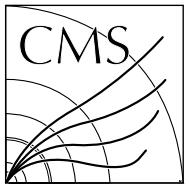

The Compact Muon Solenoid Experiment

CMS Note

Mailing address: CMS CERN, CH-1211 GENEVA 23, Switzerland

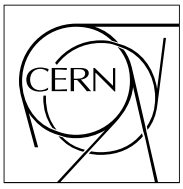

20 March 2008

Design, Performance, and Calibration of CMS Hadron Endcap Calorimeters

CMS HCAL Collaboration G. Baiatian, A. Sirunyan, I. Emeliantchik, V. Massolov, N. Shumeiko, R. Stefanovich, J. Damgov, L. Dimitrov, V. Genchev, S. Piperov, I. Vankov, L. Litov, G. Bencze, A. Laszlo, A. Pal, G. Vesztergombi, P. Zalan, A. Fenyvesi, H. Bawa, S. Beri, V. Bhatnagar, M. Kaur, J. Kohli, A. Kumar, J. Singh, B. Acharya, Sud. Banerjee, Sun. Banerjee, S. Chendvankar, S. Dugad, S. Kalmani, S. Katta, K. Mazumdar, N. Mondal, P. Nagaraj, M. Patil, L. Reddy, B. Satyanarayana, S. Sharma, K. Sudhakar, P. Verma, M. Hashemi, M. Mohammadi-Najafabadi, S. Paktinat, K. Babich, I. Golutvin, V. Kalagin, A. Kamenev, V. Konoplianikov, I. Kosarev, K. Moissenz, P. Moissenz, D. Oleynik, A. Petrosyan, E. Rogalev, R. Semenov, S. Sergeyev, S. Shmatov, V. Smirnov, A. Vishnevskiy, A. Volodko, A. Zarubin, D. Druzhkin, A. Ivanov, V. Kudinov, A. Orlov, V. Smetannikov, V. Gavrilov, Y. Gershtein, N. Ilyina, V. Kaftanov, I. Kisselevich, V. Kolossov, A. Krokhotin, S. Kuleshov, D. Litvintsev, A. Ulyanov, G. Safronov, S. Semenov, V. Stolin, A. Demianov, A. Gribushin, O. Kodolova, S. Petrushanko, L. Sarycheva, V. Teplov, I. Vardanyan, A. Yershov, V. Abramov, P. Goncharov, A. Kalinin, A. Khmelnikov, A. Korablev, Y. Korneev, A. Krinitsyn, V. Kryshkin, V. Lukanin, V. Pikalov, A. Ryazanov, V. Talov, L. Turchanovich, A. Volkov, T. Camporesi, T. de Visser, E. Vlassov, S. Aydin, M. Bakirci, S. Cerci, I. Dumanoglu, E. Eskut, A. Kayis-Topaksu, S. Koylu, P. Kurt, G. Onengut, H. Ozkurt, A. Polatoz, K. Sogut, H. Topakli, M. Vergili, T. Yetkin, K. Cankoc, A. Esendemir, H. Gamsizkan, M. Guler, C. Ozkan, S. Sekmen, M. Serin-Zeyrek, R. Sever, E. Yazgan, M. Zeyrek, M. Deliomeroglu, E. Gulmez, E. Isiksal, M. Kaya, S. Ozkorucuklu, L. Levchuk, P. Sorokin, B. Grynev, V. Lyubynskiy, V. Senchyshyn, J. Hauptman, S. Abdullin, J. Elias, D. Elvira, J. Freeman, D. Green, S. Los, V. ODell, A. Ronzhin, I. Suzuki, R. Vidal, J. Whitmore, M. Arcidy, E. Hazen, A. Heering, C. Lawlor, D. Lazic, E. Machado, J. Rohlf, F. Varela, S. X. Wu, D. Baden, R. Bard, S. Eno, T.Grassi, C. Jarvis, R. Kellogg, S. Kunori, J. Mans, A. Skuja, V. Podrasky, C. Sanzeni, D. Winn, U. Akgun, S. Ayan, F. Duru, J. Merlo, A. Mestvirishvili, M. Miller, E. Norbeck, J. Olson, Y. Onel, I. Schmidt, N. Akchurin, K. Carrell, K. Gusum, H. Kim, M. Spezziga, R. Thomas, R. Wigmans, M. Baarmand, H. Mermerkaya, R. Ralich, I. Vodopiyanov, L. Kramer, S. L. Linn, P. Markowitz, P. Cushman, Y. Ma, B. Sherwood, L. Cremaldi, J. Reidy, D. A. Sanders, D. Karmgard, R. Ruchti, W. Fisher, C. Tully, A. Bodek, P.de Barbaro, H. Budd, Y. Chung, T. Haelen, S. Hagopian, V. Hagopian, K. Johnson, V. Barnes, A. Laasanen

Abstract

Detailed measurements have been made with the CMS hadron calorimeter endcaps (HE) in response to beams of muons, electrons, and pions. Readout of HE with custom electronics and hybrid photodiodes (HPDs) shows no change of performance compared to readout with commercial electronics and photomultipliers. When combined with lead-tungstenate crystals, an energy resolution of 8% is achieved with 300 GeV/c pions. A laser calibration system is used to set the timing and monitor operation of the complete electronics chain. Data taken with radioactive sources in comparison with test beam pions provides an absolute initial calibration of HE to approximately 4% to 5%.

CMS HCAL Collaboration

G. Baiatian, A. Sirunyan

Yerevan Physics Institute, Yerevan, Armenia

I. Emeliantchik, V. Massolov, N. Shumeiko, R. Stefanovich

NCPHEP, Minsk, Belarus

J. Damgov, L. Dimitrov, V. Genchev, S. Piperov, I. Vankov

Institute for Nuclear Research and Nuclear Energy, Bulgarian Academy of Science, Sofia, Bulgaria

L. Litov

Sofia University, Sofia, Bulgaria

G. Bencze, A. Laszlo, A .Pal, G. Vesztergombi, P. Zalan

KFKI-RMKI, Research Institute for Particle and Nuclear Physics, Budapest, Hungary

A. Fenyvesi

ATOMKI, Debrecen, Hungary

H. Bawa, S. Beri, V. Bhatnagar, M. Kaur, J. Kohli, A. Kumar, J. Singh

Panjab University, Chandigarh, 160 014, India

B. Acharya, Sud. Banerjee, Sun. Banerjee, S. Chendvankar, S. Dugad, S. Kalmani, S. Katta, K. Mazumdar, N. Mondal, P. Nagaraj, M. Patil, L. Reddy, B. Satyanarayana, S. Sharma, K. Sudhakar, P .Verma

Tata Institute of Fundamental Research, Mumbai, India

M. Hashemi, M. Mohammadi-Najafabadi, S. Paktinat

Institute for Studiesin Theoretical Physics and Mathematics and Sharif University of Technology, Tehran, Iran

K. Babich, I. Golutvin, V. Kalagin, A. Kamenev, V. Konoplianikov, I. Kosarev, K. Moissenz, P. Moissenz, D. Oleynik, A. Petrosyan, E. Rogalev, R. Semenov, S. Sergeyev, S. Shmatov, V. Smirnov, A. Vishnevskiy, A. Volodko, A. Zarubin

JINR, Dubna, Russia

D. Druzhkin, A. Ivanov, V. Kudinov, A. Orlov, V. Smetannikov

High Temperature Technology Center of Research & Development Institute of Power Engineering, Moscow, Russia

V. Gavrilov, Y. Gershtein[1)], N. Ilyina, V. Kaftanov, I. Kisselevich, V. Kolossov, A. Krokhotin, S. Kuleshov, D. Litvintsev[2)], A. Ulyanov, G. Safronov, S. Semenov, V. Stolin
ITEP, Moscow, Russia

A. Demianov, A. Gribushin, O. Kodolova, S. Petrushanko, L. Sarycheva, V. Teplov, I. Vardanyan, A. Yershov

Moscow State University, Moscow, Russia

V. Abramov, P. Goncharov, A. Kalinin, A. Khmelnikov, A. Korablev, Y. Korneev, A. Krinitsyn, V. Kryshkin, V. Lukanin, V. Pikalov, A. Ryazanov, V. Talov, L. Turchanovich, A. Volkov
IHEP, Protvino, Russia

T. Camporesi, T. deVisser, E. Vlassov[3)]

CERN, Geneva, Switzerland

S. Aydin, M. Bakirci, S. Cerci, I. Dumanoglu, E. Eskut, A. Kayis-Topaksu, S. Koylu, P. Kurt, G. Onengut, H. Ozkurt, A. Polatoz, K. Sogut, H. Topakli, M. Vergili, T. Yetkin

Cukurova University, Adana, Turkey

K. Cankocak[4)], A. Esendemir, H. Gamsizkan, M. Guler, C. Ozkan, S. Sekmen, M. Serin-Zeyrek, R. Sever, E. Yazgan, M. Zeyrek

Middle East Technical University, Ankara, Turkey

M. Deliomeroglu, E. G¨ulmez, E. Isiksal[5)], M. Kaya[6)], S. Ozkorucuklu[7)]

Bogazici University, Istanbul, Turkey

L. Levchuk , P. Sorokin

KIPT, Kharkov, Ukraine

B. Grynev, V. Lyubynskiy, V. Senchyshyn

Institute for Scintillation Materials NASU, Kharkov, Ukraine

J. Hauptman

Iowa State University, Ames, IA, USA

S. Abdullin, J. Elias, D. Elvira, J. Freeman, D. Green, S. Los, V. O'Dell, A. Ronzhin, I. Suzuki, R. Vidal, J. Whitmore

Fermi National Accelerator Laboratory, Batavia, IL, USA

M. Arcidy, E. Hazen, A. Heering, C. Lawlor, D. Lazic, E. Machado, J. Rohlf, F. Varela, S. X. Wu

Boston University, Boston, MA, USA

D. Baden, R. Bard, S. Eno, T. Grassi, C. Jarvis, R. Kellogg, S. Kunori, J. Mans[8)], A. Skuja

University of Maryland, College Park, MD, USA

V. Podrasky, C. Sanzeni, D. Winn

Fairfield University, Fairfield, CT, USA

U. Akgun, S. Ayan, F. Duru, J. Merlo, A. Mestvirishvili, M. Miller, E. Norbeck, J. Olson, Y. Onel, I. Schmidt

University of Iowa, Iowa City, IA, USA

N. Akchurin, K. Carrell, K. G¨usum¨, H. Kim, M. Spezziga, R. Thomas, R. Wigmans

Texas Tech University, Lubbock, TX, USA

M. Baarmand, H. Mermerkaya, R. Ralich, I. Vodopiyanov

Florida Institute of Technology, Melbourne, FL, USA

L. Kramer, S.L. Linn, P. Markowitz

Florida International University, Miami, FL, USA

P. Cushman, Y. Ma, B. Sherwood

University of Minnesota, Minneapolis, MN, USA

L. Cremaldi, J. Reidy, D. A. Sanders

University of Mississippi, Oxford, MS, USA

D. Karmgard, R. Ruchti

University of Notre Dame, Notre Dame, IN, USA

W. Fisher, C.Tully

Princeton University, Princeton, NJ, USA

A. Bodek, P.de Barbaro, H. Budd, Y. Chung, T. Haelen

University of Rochester, Rochester, NY, USA

S. Hagopian, V. Hagopian, K. Johnson

Florida State University, Tallahassee, FL, USA

V. Barnes, A. Laasanen

Purdue University, West Lafayette, IN, USA

[1)] Now at Florida State University, Tallahassee, FL, USA.
[2)] Now at FNAL, Batavia, IL, USA.
[3)] Also with ITEP, Moscow, Russia.
[4)] At Mugla University, Mugla, Turkey.
[5)] At Marmara University, Istanbul, Turkey.
[6)] At Kafkas University, Kars, Turkey.
[7)] At Suleyman Demirel University, Isparta, Turkey.
[8)] Now at University of Minnesota, Minneapolis, MN, USA.

1 Introduction

The CMS detector (Figure 1) is designed to study a wide range of fundamental problems involving diverse signatures with final states containing muons, electrons, photons, hadron jets and neutrinos or exotic particles resulting in apparent missing energy [1]. The hadron calorimeter (HCAL) endcaps (HE) [2] cover a substantial portion of the rapidity range, $1.3 < |\eta| < 3$ (13.2% of the solid angle), a region containing about 34% of the particles produced in inclusive final states. The high luminosity of the LHC (10^{34} cm^{-2} s^{-1}) requires HE to handle high (MHz) counting rates and have high radiation tolerance (10 Mrad after 10 years of operation at design luminosity).

It is not physically possible to place the entire hadron calorimeter in the test beam to obtain calibtarion constants for every tower. Instead a radioactive source measures the response of the active elements and is compared to beam measurements in a 20^{rmo} segment and verified in the test beam that transfering calibration constants from raioactive source to beam is good to a few percent accuracy.

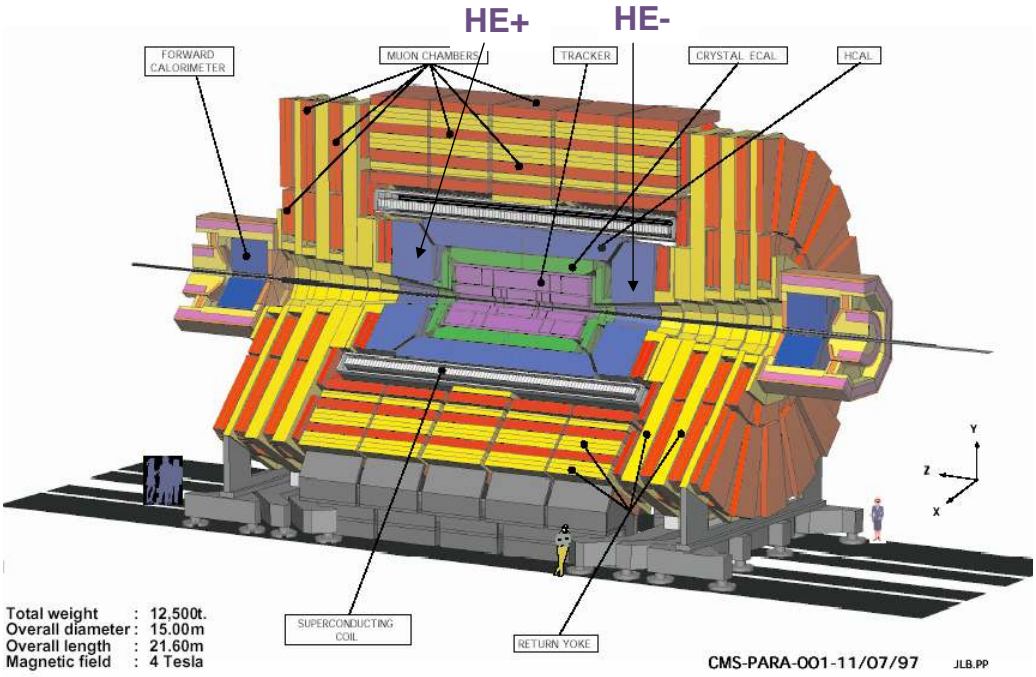

Figure 1: General view of the CMS Detector indicating the location of hadron calorimeter end caps, HE+ and HE- at $+z$ and $-z$.

2 HCAL Endcap Design

The HE is a sampling calorimeter similar to that of the hadron barrel (HB) [3]. Since the calorimeter is inserted into the ends of a 4 T solenoidal magnet, the absorber must be made from a nonmagnetic material having maximum absorption length, good mechanical properties and reasonable cost, leading to the choice of C26000 cartridge brass (70% Cu and 30% Zn), density 8.83 gm/cm^3, interaction length of 16.4 cm and radiation length of 1.5 cm. The endcaps are attached to the muon end cap yoke as shown in Figures 2 and 3. Only a small part of the calorimeter structure can be used for fixing to the magnet iron, as most of the space between HE and the muon absorber is occupied with muon cathode strip chambers. A 10 t electromagnetic calorimeter with a 2 t preshower detector is attached to the front face of HE. The large weight involved (about 300 t) and a strict requirement to minimize non-instrumented material along particle trajectories, has made the design of HE an unprecedented challenge to engineers. An interface was designed in order to provide precise positioning of the endcap detectors with respect to the adjacent muon iron, and to minimize the influence of deformation under magnetic forces. The interface contains a sliding joint between the interface tube, and an HE back-flange with a hinged connection between brackets and the iron disk (YE1). Introduction of the interface sliding support into the design reduces the forces and stresses in the brackets, back flange and brass bolts. Structural materials used in the interface system are non-magnetic in order not to distort the axial magnetic field.

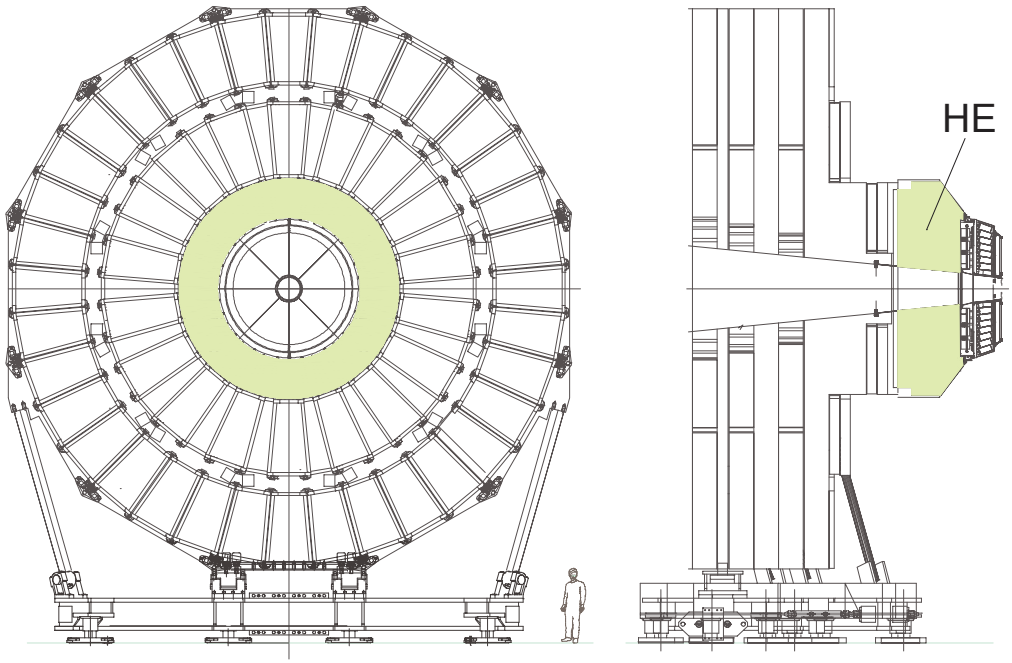

Figure 2: Hadron endcap calorimeter mounted on the endcap iron yoke.

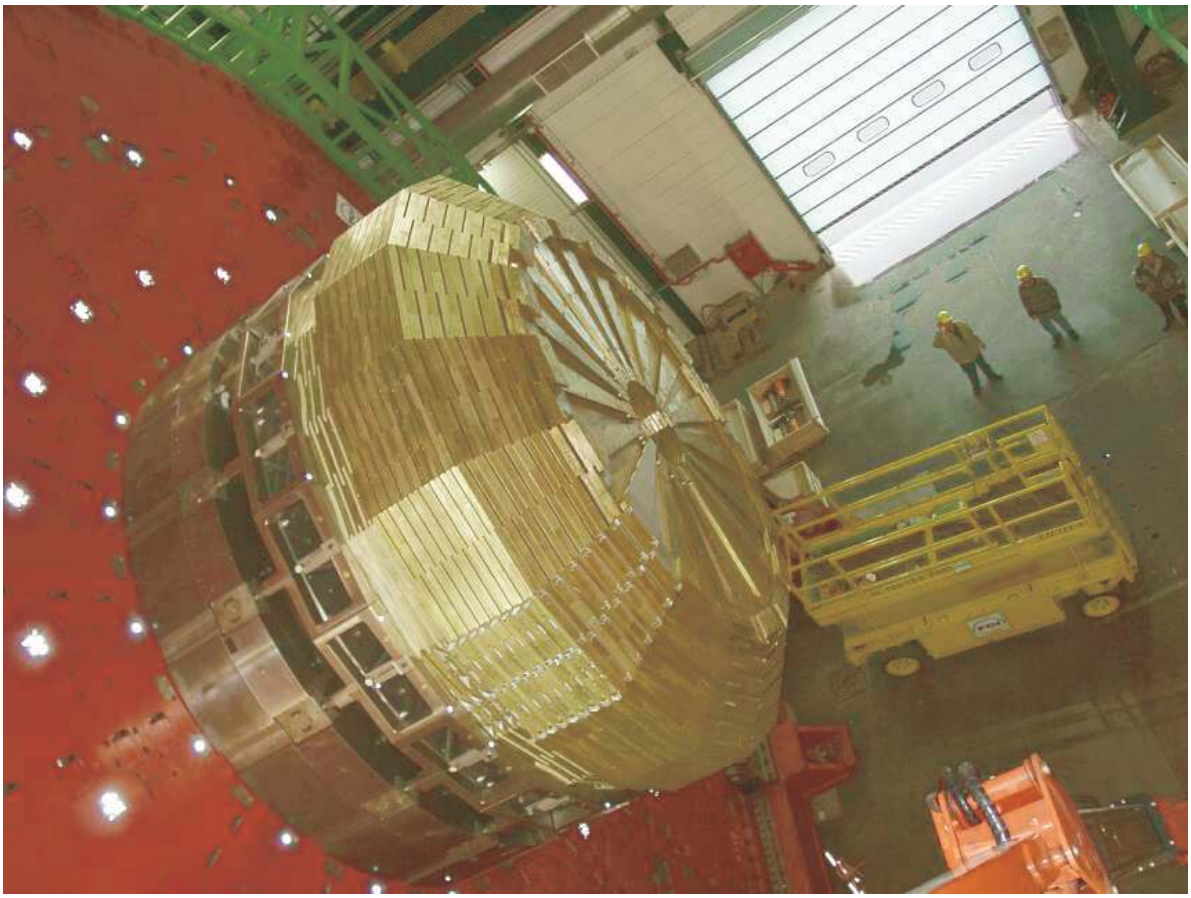

Figure 3: Partially assembled HE calorimeter in the CMS surface hall (SX5).

2.1 Absorber Geometry

The detailed design of the absorber minimizes the cracks between the HB and HE. The cracks are made non projective so the energy of jet of particles in the crack direction can be measured. In this area energy resolution of jets is limited by pileup, magnetic field effects, and parton fragmentation [4, 5]. The plates are bolted together in a staggered geometry resulting in a configuration that contains no projective "dead" region (see Figure 4). The design is self supporting and can be readily assembled and disassembled for transportation. The brass plates are 79 mm thick with 9 mm gaps to insert the scintillator tiles. The total interaction length of the calorimeter, including electromagnetic crystals, is about 10 λ_{I}.

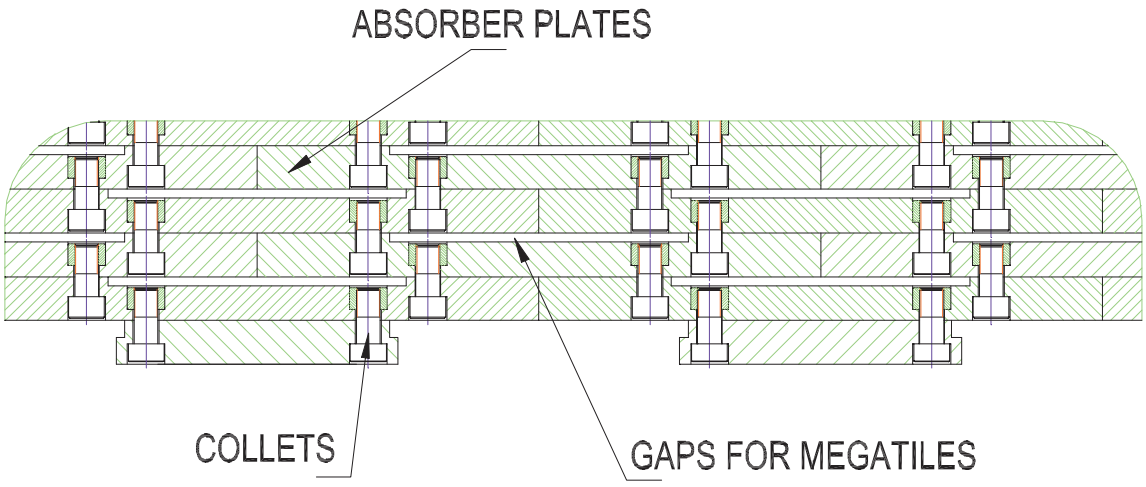

Figure 4: Mechanical structure of the HE absorber. Particles enter the calorimeter from the bottom.

The outer layers of the HE are cut out for installation of the photodetectors and front end electronics. To compensate for the resulting reduction of material, an extra layer (–1) is added to tower 16 [3]. The outer layers are fixed to a 10 cm thick stainless steel support plate. The optical elements are inserted into the gaps after the absorber is assembled. Therefore the optical elements must have a rigid structure to allow for insertion in any orientation.

2.2 Scintillator Trays

The scintillation light is collected by wavelength shifting fibers (WLS), inseted in machined groves near the perifery of the scintillator [6, 7]. The advantage of this design minimizes of dead regions since the light can be easily routed to the photodetectors by a 0.94 mm fiber. Trapezoidal-shaped scintillators (Figure 5) are 4.0 mm thick SCSN81 or 9 mm thick Bicron BC408 for Layer-0, have grooves in which the WLS are inserted. The ends of the fibers are machined with a diamond fly cutter and one end is aluminized by sputtering to increase the light collection. The other end is spliced to a clear fiber, which is glued in a custom made optical connector. The face of the connector is also machined using a diamond fly cutter. The scintillator is painted white along the narrow edges and put into a frame to form a tray. The total number of tiles for both HE calorimeters is 20,916 and the number of trays is 1,368. The design of a tray is shown in Figure 6. The numbering system in η is shown in Figure 7 and the CMS convention for ϕ as applied to the HE and is shown in Figure 8. The scintillators are wrapped with Tyvek and sandwiched between sheets of duraluminum. The stack contains holes for fibers which are terminated with optical connectors. The gap between the aluminum plates is fixed by brass spacers screwed together. The granularity of the HE is $\Delta\eta \times \Delta\phi = 0.087 \times 0.087$ for $|\eta| < 1.6$ and $\Delta\eta \times \Delta\phi \approx 0.17 \times 0.17$ for $|\eta| \geq 1.6$.

The tray design is robust and reliable. The trays are relatively stiff which is very important for insertion into the abosrber. To control the scintillator tray quality, a UV nitrogen laser was used to excite the scintillators. The light is fed by quartz fibers to the connector and is fanned out as shown in Figure 6. These fibers are terminated with aluminum reflectors and distribute the light to each tile. The light signal produced by a UV flash in the scintillator is similar to the signal induced by a charged particle. This allows a performance check of the entire optical route from scintillator to electronics, providing a means to monitor possible degradation of transparency due to radiation damage. For further calibration and monitoring, a radioactive source on the tip of a wire moves in a stainless steel tube. This radiation measurement relative to test beam measurements is used to transfer the calibration coefficients of the HE units that were not placed in the test beam.

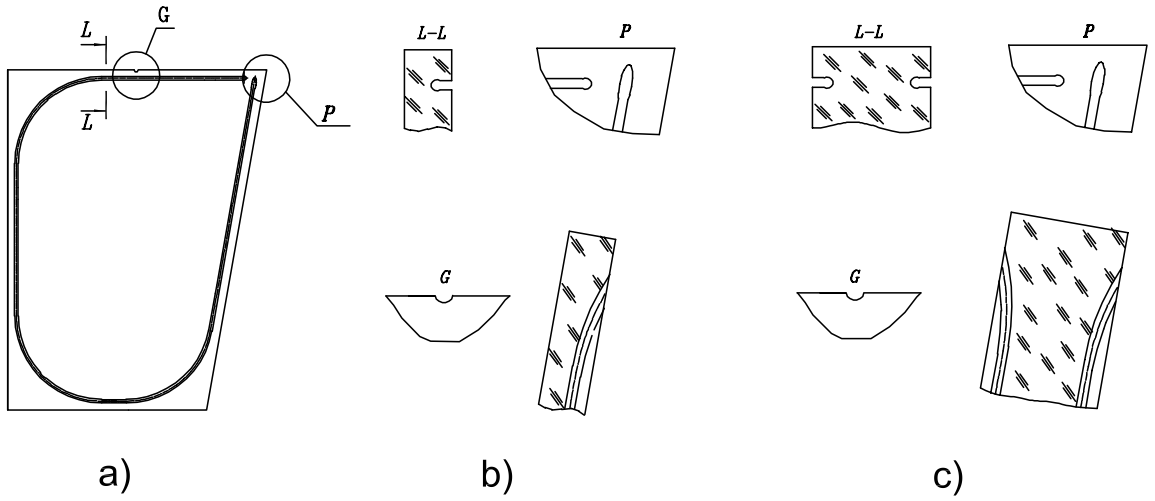

Figure 5: a) Basic structure of a scintillator tile with a groove to fix the wavelength shifting fiber, b) cross section of the 4 mm thick scintillator for layers 1-17, and c) cross section of the 9 mm thick scintillator for Layer-0. Two layers of reflecting paint cover the side surfaces of the tile.

The trays are inserted into the gaps in the absorber and fixed in position by screws. At the back of the calorimeter, near the crack are located the readout boxes (RBX) where photodetectors and front end electronics are located. Optical cables transfer signals from the scintillators trays to the phototdetectors. Multipixel hybrid photodiodes (HPDs) are used as photodetectors due to their low sensitivity to magnetic fields and and their large dynamic range.

2.3 Longitudinal Segmentation

The longitudinal segmentation of HE (Figure 9) is, in part, motivated by the fact that the front ends facing the center of CMS will suffer some radiation damage and the calibration coefficients can be corrected due to the scintillator light loss. This procedure will restore the energy resolution of the HE for the lifetime radiation dose of CMS. The towers nearest the beam line (tower 28) have transverse division (28 plus guard ring ”29”) and 3 divisions in depth which are readout separately. The other towers (except 16 and 17 which overlap with the electromagnetic barrel calorimeter) have two longitudinal readouts segmentation for potential use during the time period when when the electromagnetic endcap calorimeter (EE) may not yet be available. A special scintillator layer of 9 mm BC408 (Layer-0) is installed in front of the absorber to partially correct for the different response of the EE to electrons and hadrons and for particle absorption in the mechanical structure supporting the EE.

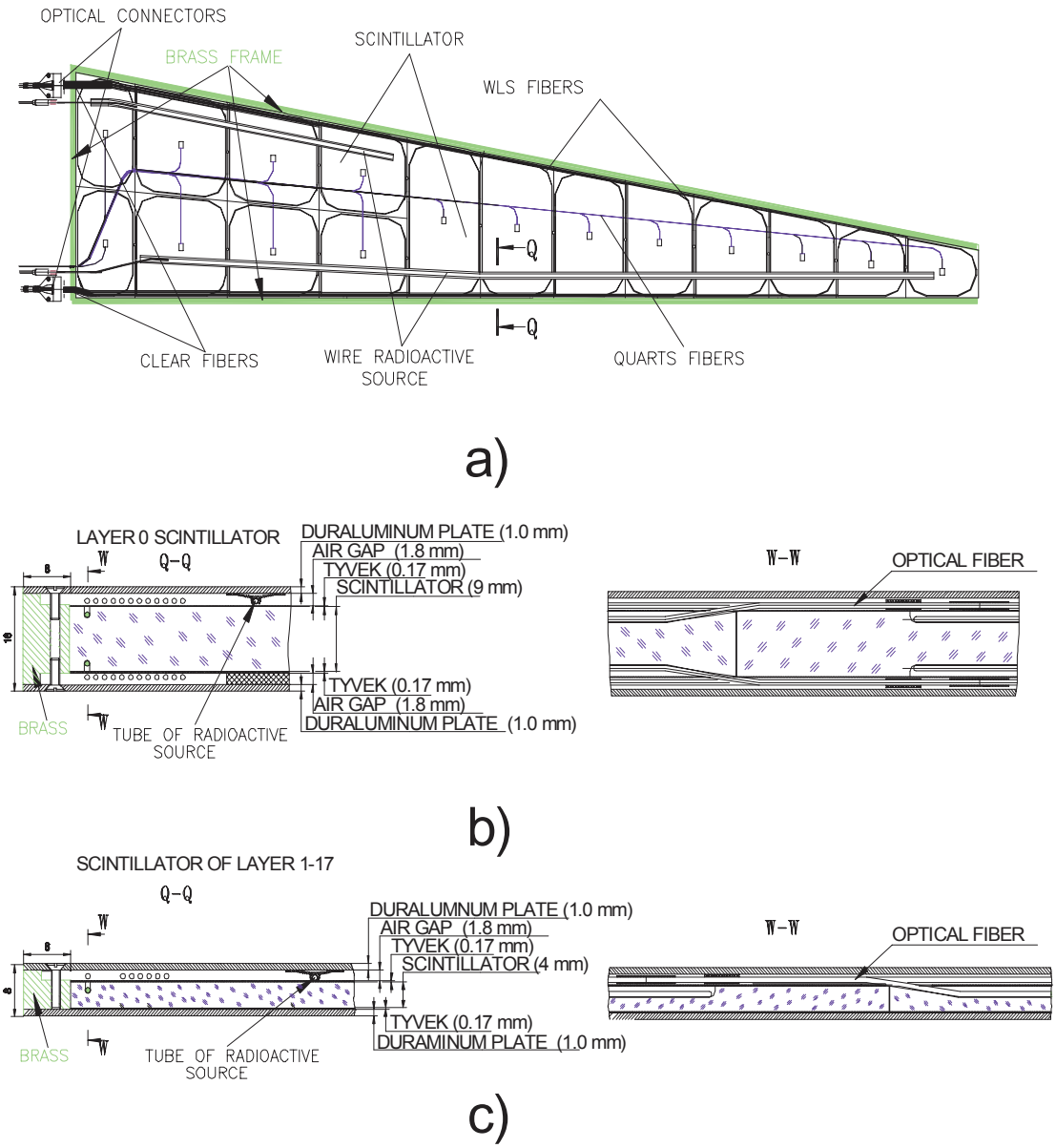

Figure 6: The design of the calorimeter scintillator trays: a) front view of a tray without the upper aluminium cover, b) cut out view of the layer-0 tray with two fibers from a tile, c) cut out view of a tray for layers 1-17.

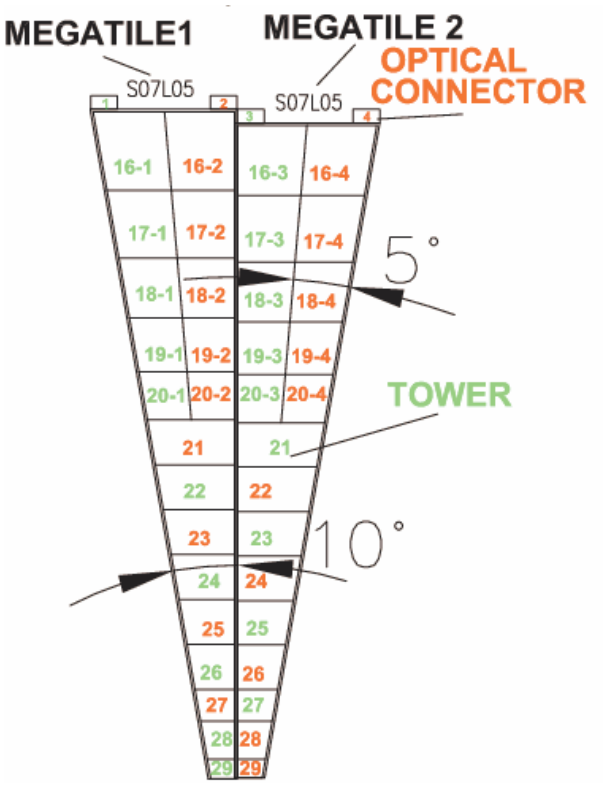

Figure 7: Numbering scheme for the tiles in adjacent scintillator trays.

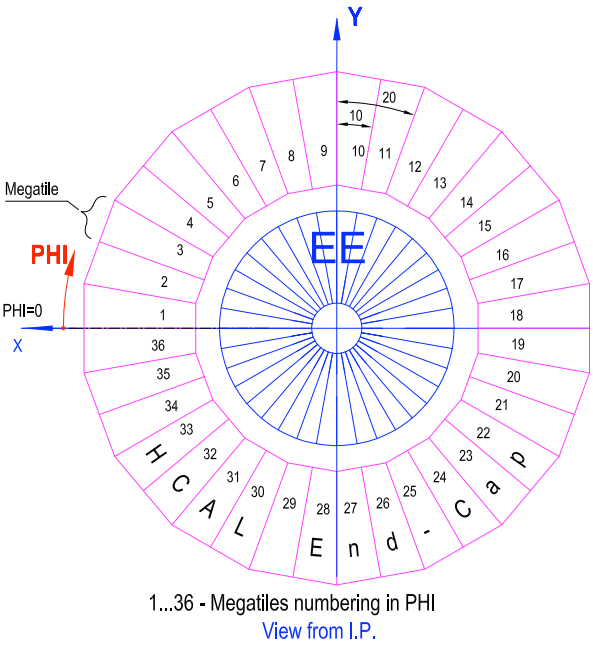

Figure 8: Numbering scheme for the HE wedges as viewed from the interaction point. The $+x$ direction points to the center of the LHC ring.

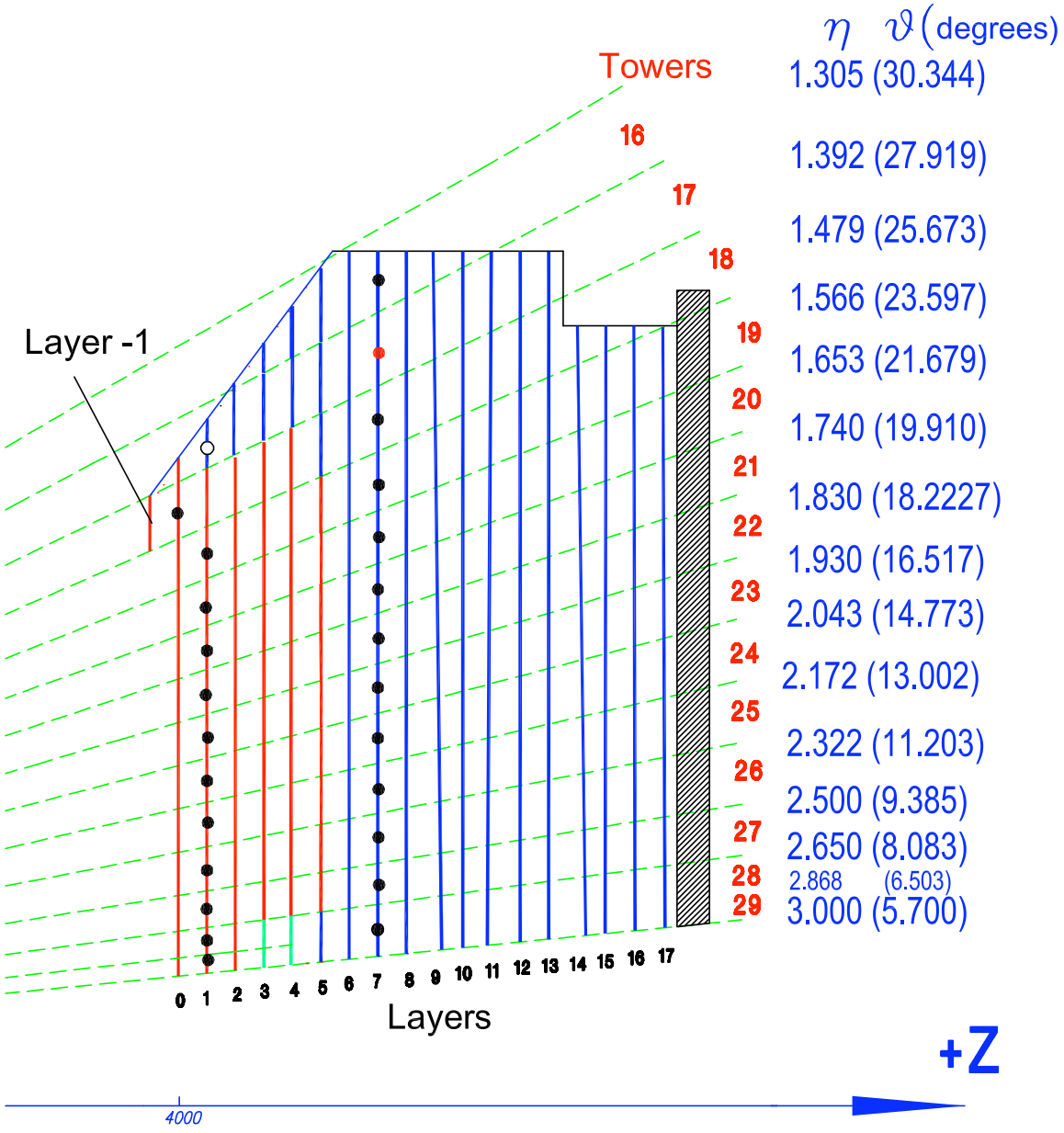

Figure 9: Longitudinal and polar angle segmentation of the HE calorimeter. The dashed lines are directed at the interaction point.

3 Performance with Photomultipliers

The HE characteristics were studied with a sector prototype which has been "permanently" installed in the CERN H2 test beam. The sector was mounted on a rotating table [3]. The two-dimensional movement of the platform (Figure 10) allowed the beam to be directed onto any desired location in η, ϕ space. The position of the platform was measured electronically and recorded in the data stream. The detector readout also provided an accurate measurement of the detector position with respect to the beam. The beam line was equipped with four 1 cm thick scintillator counters for triggering and two sets of wire chambers to measure event-by-event the position of incident particles.

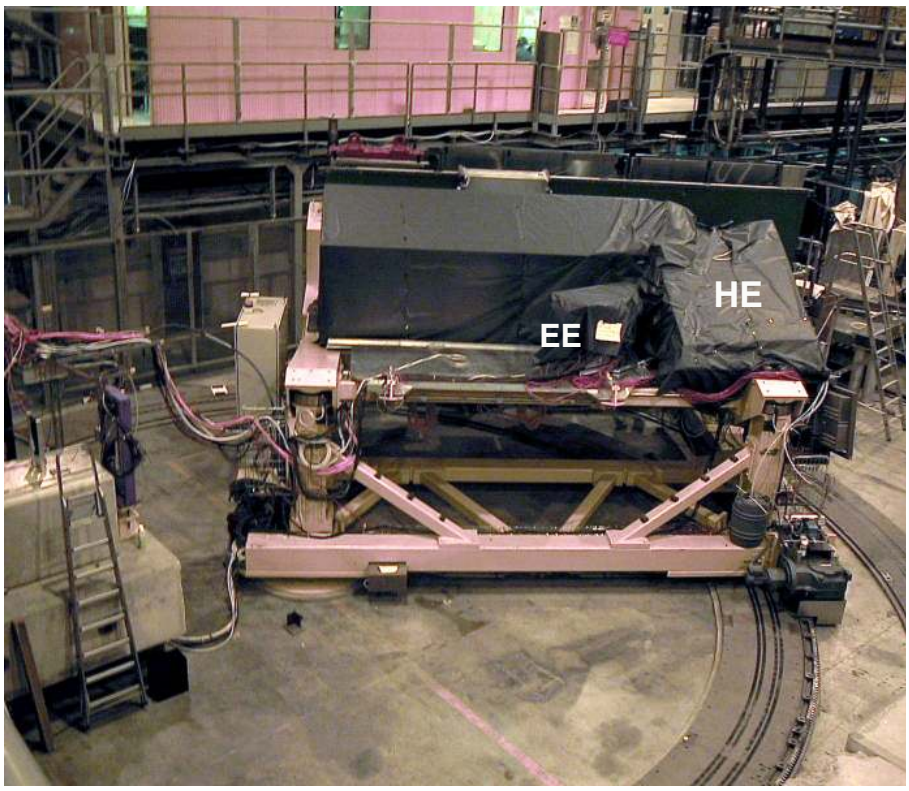

Figure 10: HE sector prototype and the EE test beam module mounted on the moving platform.

During a muon scan, the light from an irradiated tower was collected with a single photomultiplier (FEU 85). The light from Layer-0 was fed to a separate photomultiplier, also type FEU 85. During a pion scan, light from 4 towers (19 and 20) was collected with a photomultiplier (RCA 8579). The light from tower 21 was also fed into a separate FEU 85 photomultiplier to estimate transverse shower leakage. Basically, only these towers provide sufficient transverse containment to an incident pion beam. The beam was further positioned at the center between towers 19 and 20 to ensure minimal transverse pion shower leakage. There was additional information recorded by a muon counter placed behind the HE in order to tag and/or veto muons in the H2 beam line.

3.1 Energy Calibration

The energy calibration, ADC counts to GeV, was determined with pion beams in the momentum range of 20-300 GeV/c. At the analysis stage, events muon tags were rejected. There were also requirements that the distance between the beam center and the particle trajectory observed in the wire chambers must be in the range from +5 mm to –15 mm and the difference of the coordinate in the first and the second wire chamber must be less than 3 mm. The leakage from the calorimeter in the transverse direction was estimated using information from tower 21. The signals from tower 21 were added to the signals from the main part of the calorimeter with a relative weight optimized to obtain the best energy resolution.

From these measurements, the energy calibration was measured to be 0.11 GeV per ADC count of course dependent on the high voltage on the photo multiplier tubes.

The calibration response was defined by normalizing the energy deposited into the center 4 towers for 300 GeV/c

pions, without taking into account the response of tower 21. Figure 11 shows the energy resolution (σ) versus the beam energy (E) and fitted to the function $A/\sqrt{E} \oplus B$ where E is in GeV, with stochastic term $A = 1.02$ GeV$^{1/2}$ and constant term $B = 0.027$ folded in quadrature (denoted by the symbol $\oplus$). Applying the calibration to the muon beam data, the mean muon energy deposited in the calorimeter was measured to be 3.53 GeV.

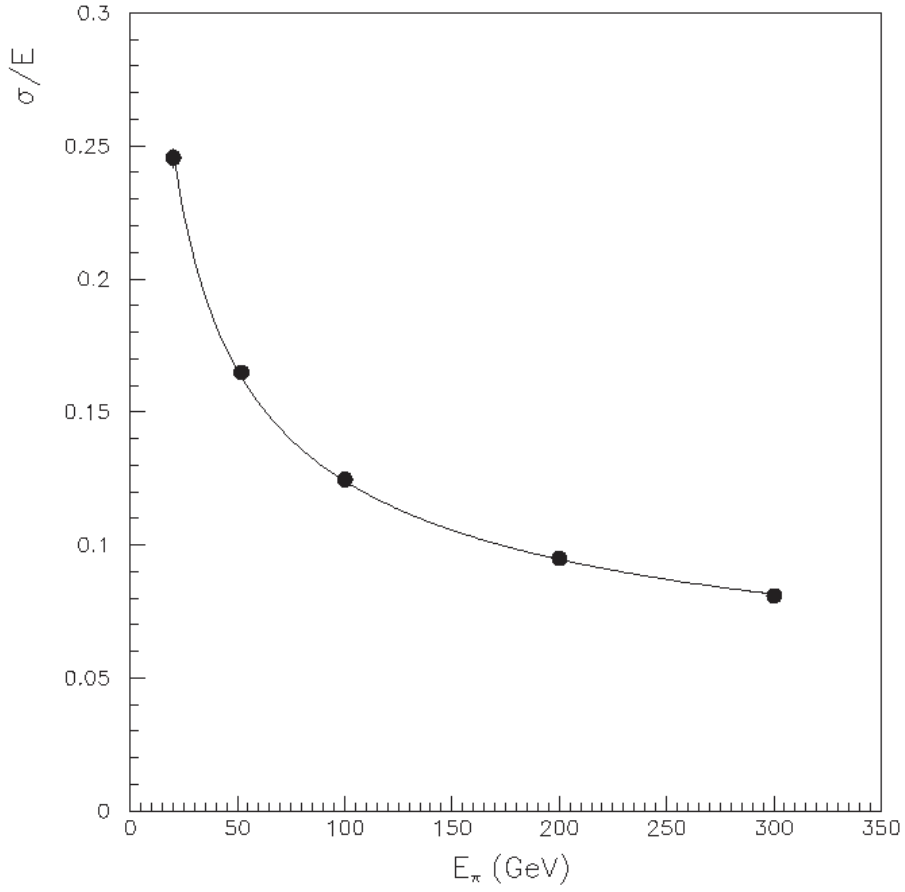

Figure 11: Fractional energy resolution of HE as a function of beam energy. EE was not in place in front of HE.

3.2 Muon Signal

Figure 12 shows the ADC distribution from muons in Layer-0. The solid line shows the distribution fitted to a Poisson-Gaussian-Landau convolution. The estimated most probable average number of photoelectrons (PE) is 13. Taking into account that one ADC count is equal to 3.7 fC, we have 10.4 fC/photoelectron. The muon signal from a full tower corresponds to 55 photoelectrons. Since a tower consists of 17 scintillator layers, a single layer produces 3.2 PE per muon.

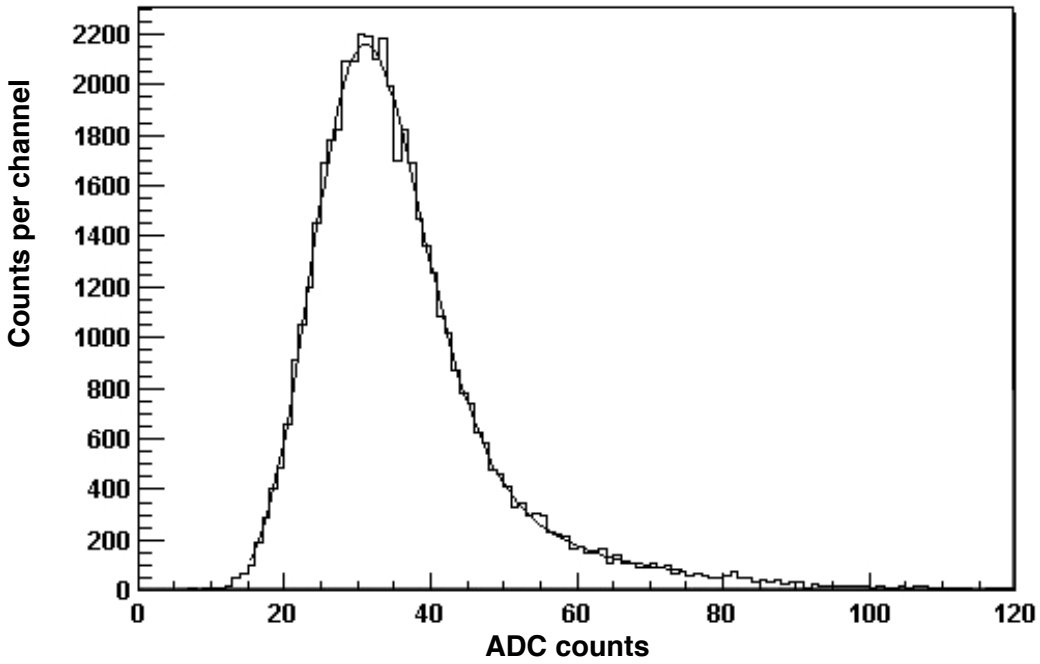

Figure 12: Muon pulse-height distribution from Layer-0.

3.3 Pulse Shape

The pulse duration of the HE defines its operating speed. There are the following contributions:

1. the time decay of the scintillator is about 5 ns for the SCSN81 scintillator manufactured by Kuraray;
2. the time to re-emit light by the wavelength shifted fibrt is 11 ns for the Y11 manufactured by Kuraray;
3. the difference in optical length from different tiles to the photodetector for a tower, estimated to be 1 ns with time-of-flight taken into account; and
4. the pulse width from the scintillator is defined by the time collection of the slow neutrons in the hadron shower.

For this study, the FEU 85 phototube was used which has an intrinsic pulse width of 10 ns. The muon pulse shape from the 17 layers of an HE tower and the pulse length from a single scintillator excited by the UV laser pulse (5 ns duration) are approximately the same (about 30 ns). The bulk (over 95% of the HE signal is collected in two beam crossing periods, or 50 ns.

3.4 Performance with ECAL

The CMS combined calorimeter consists of the endcap electromagnetic calorimeter (EE) of lead-tungstenate crystals followed by HE. The front part of HE contains a special scintillator (Layer-0) used to sample the energy of the hadron shower in EE. Because the hadronic to electromagnetic response ratio (h/e) is smaller for EE than for HE,

there is a degradation of energy resolution of the combine calorimeter in comparison with the HE energy resolution alone (see Figure 11) [3].

CMS production Electromagnetic Calorimeter modules were not available at the time of these test beam measurements. Instead the measurements used lead glass SF5 calorimeter from experiment WA91 [9] that is a sufficient approximation of the lead tungstate crystals. The calorimeter has dimensions $14 \times 14 \times 47\,\mathrm{cm}^3$ which is 18.5 radiation lengths in depth. Light was collected by a XP-2050 phototube. The energy resolution of the calorimeter obtained by the WA91 collaboration is described by the expression $\sigma(E)/E = A/\sqrt{E} \oplus B$, where E is in GeV. The constants are $A = 5.8 \times 10^{-2}\ \mathrm{GeV}^{1/2}$, $B = 1.4 \times 10^{-2}$ and the symbol $\oplus$ denotes addition in quadrature. The response of the electromagnetic calorimeter depends linearly on electron energy. The energy response (E) of the combined calorimeter was calculated according to the following expression:

$$E = W_1 E_E + E_H + W_2 E_0 + W_3 E_{21},$$

where E_E and E_H are the energies observed in the lead glass approximation to EE and HE, respectively, E_0 is the energy measured in Layer-0, E_{21} is the energy from tower 21 which is adjacent to the towers used to measure E_H, and the weighing factors W_1, W_2, and W_3 are free parameters. The weights W_1, W_2, and W_3 were optimized for each beam energy to minimize the energy resolution, $\sigma(E)/E$. The term $W_3 E_{21}$ in the above expression is the estimate of the transverse leakage of the hadron shower. The laser control system was used to correct for the nonlinearity of the phototubes. The total response of the combined calorimeter is presented in Figure 13 for an incident 300 GeV pion beam. The Gaussian form gives an acceptible fit.

The energy resolution of the combined calorimeter is presented in Figure 14, where the solid line is the fit to the expression $\sigma(E)/E = A/\sqrt{E} \oplus B$. The fit parameters are $A = 1.53 \pm 0.04\ \mathrm{GeV}^{1/2}$ and $B = 0.063 \pm 0.005$. Note that the EE has significantly degraded the pion resolution compared to the response of HE alone (Figure 11).

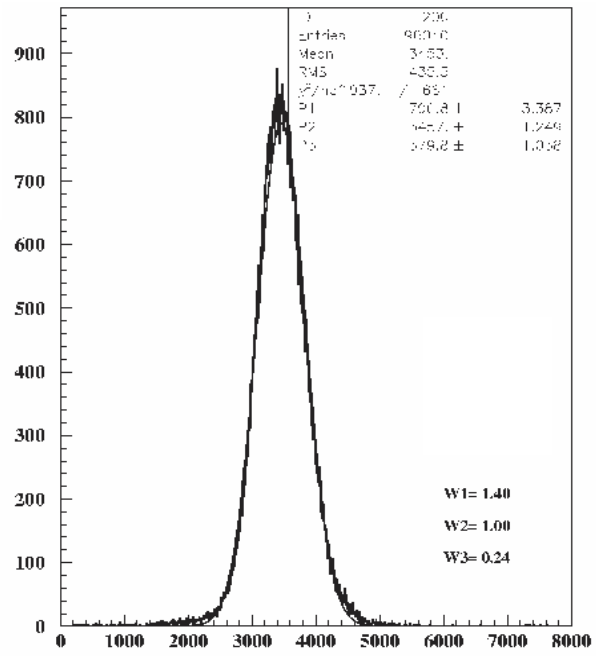

Figure 13: Energy distribution from the combined calorimeter for 300 GeV/c pions (in arbitrary units).

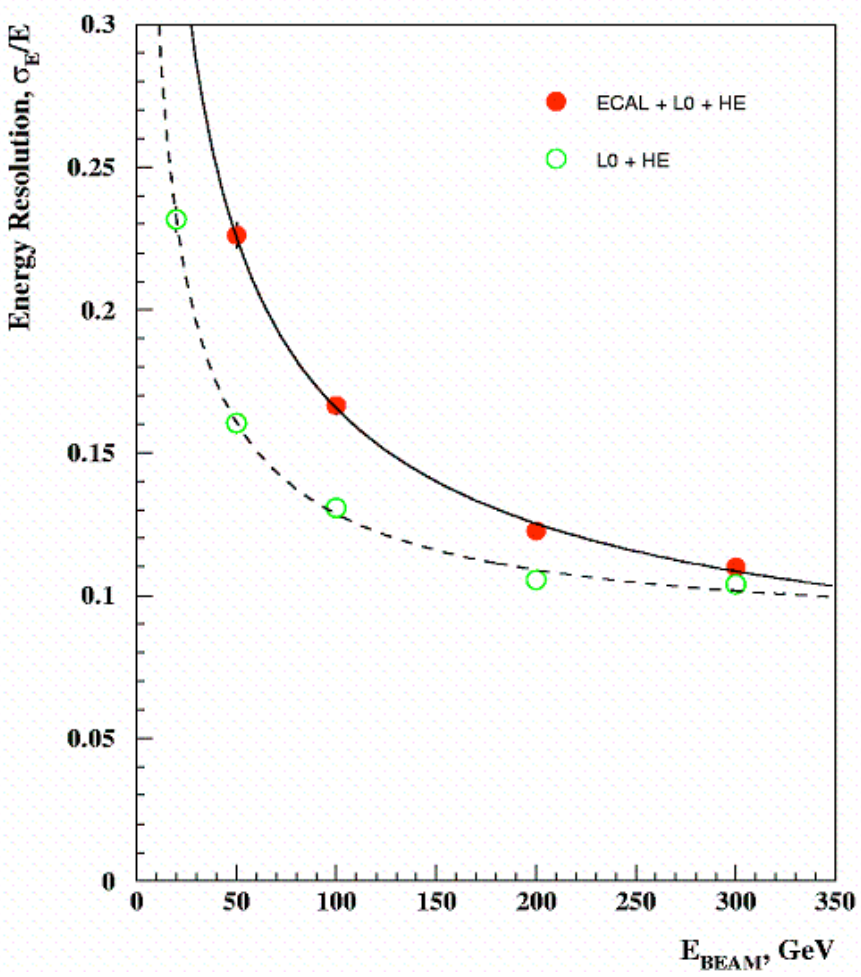

Figure 14: Fractional energy resolution of the combined calorimeter as a function of the pion beam energy.

3.5 Layer-0 Weight

The energy dependence of the combined calorimeter resolution on the weight of Layer-0 is presented in Figure 15 for beam energies of 50, 100, 200 and 300 GeV. The difference in phototubes gains was corrected by measuring the responses to a muon beam for each part of the combined calorimeter. As one can see from Figure 15, the optimal weight for Layer-0 lies within a small range for all beam energies, and the average of the transmission coefficient is about 0.23. Because of this weak energy dependence this transmission value can then be used in passively summing (optically) an attenuated Layer-0 signal with the rest of HE. Since the characteristics of the electromagnetic calorimeter used for this measurement differ from the CMS electromagnetic calorimeter, the obtained weight must be considered to be an initial estimate. Further measurements are planned when CMS prototypes of EE become available. We are also investigating alternative methods to sum up EE and HE energies [10].

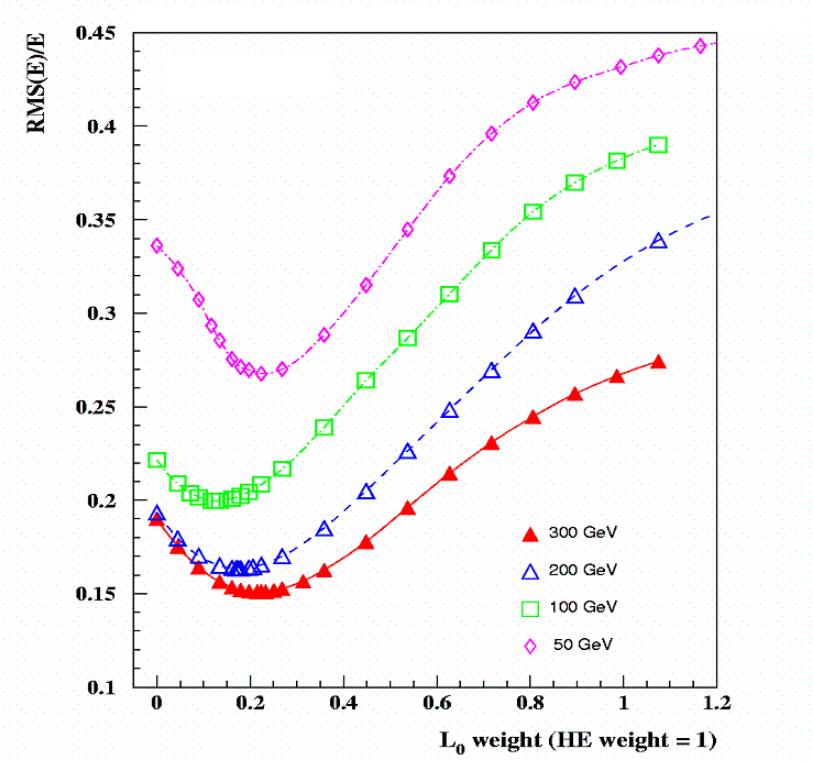

Figure 15: Energy-resolution dependence of the combined calorimeter fractional energy resolution on layer-0 weight.

As mentioned above, the relevant conversion factors for the HE are: 1 ADC count = 3.7 fC, 1 PE = 10.4 fC, and 1 ADC count = 0.11 GeV. Using these factors, HE produces 25 PE per GeV. Therefore, photostatistics do not

significantly contribute to the stochastic coefficient because that term $0.2/\sqrt{E}$ which is folded in quadrature with a term approximately 5 times larger. The first layer, Layer-0, is thicker (9mm *vs.* 4 mm) and brighter (Bicron BC408 *vs.* SCSN81) so that using Layer-0 in the optical sum of layers for HE does not alter this conclusion, even after the optimal attenuation of the Layer-0 light by a factor of 0.23 (see Figure 15).

The CMS calorimeter contains construction material to fasten EE to HE in addition to the photodetectors, electronics, cooling and other inert material. To study the influence of these structures on the energy resolution of the combined calorimeter, an aluminum bar with cross section $25 \times 25\ \mathrm{mm}^2$ and length 150 mm was placed between EE and HE. The supporting structures between EE and HE will not exceed the bar dimensions in regards to the number of interaction lengths. The observed decrease of the HE response when the bar is put into the beam is compensated by an increase in the layer-0 response. The total response of the combined calorimeter did not change within the measurement errors. This conclusion must be checked in the test beam when final production EE modules become available for testing.

4 HE Performance with HPDs and Production Electronics

The studies of the HE prototype described above was performed with photomultipliers. When final electronics [11] and hybrid photodiodes (HPDs) [12] became available, another series of measurments were performed in the test beam. The HE response with final electronics and HPD's was studied with the absorber prototype (Figure 10) installed on the CERN H2 test beam. A prototype lead-tungtunate electromagnetic calorimeter (EEP) with 49 crystals was used in front of HE [3], but it was read out using phototubes.

Scintillator performance was monitored by radioactive source tubes and a light injection system. The stand-alone HE was exposed to electrons of 5, 9, and 100 GeV, pions at 5, 9, 50, 100, 150, 300 GeV, and muons of 150 GeV. The HE+EEP was exposed to electrons of 50 and 100 GeV, pions of 30, 50, 100, 150, 300 GeV, and muons of 150 GeV.

4.1 Muon and Electron Response

The timing charateristics of HE are well understood [13]. For these measurements, the HE signal was summed over five 25 ns time samples, assuring total signal collection. Figure 16 shows a pedestal distribution for a single tower. The fitted spread is $\sigma = 0.38$ GeV. The variation of the pedestal mean during the measurements was less than 0.1%. Figure17 shows the pedestal subtracted pulse height distribution for 150 GeV incident muons. The muon response measured with HPDs is very similar to that obtained with photomultipliers which confirms that the production electronics does not introduce additional noise. Figure18 shows the signal from 100 GeV electrons.

4.2 Response to Pions

Because the HE sector prototype has limited transverse dimensions (two 10° sectors, see Figure 7), there was an appreciable transverse shower leakage. The value of the leakage was estimated by measuring the ratio $(E_{16} - E_9)/E_{16}$ as shown in Figure 19, where E_{16} (E_9) is the energy in a 4×4 (3×3) 5° tower array. Data are shown both with and without EEP. From these measurements the average energy leakage can be determined. Fluctuations are not accounted for note that the mean values of $(E_{16} - E_9)/E_{16}$ are less than the measured energy resolutions (see Figure 14).

An important characteristic of the calorimeter is the pion to electromagnetic (π/e) energy-dependent response ratio, which is parameterized by the expression:

$$\frac{\pi}{\mathrm{e}} = 1 - (1 - \tfrac{1}{e/h})(E/E_0)^{m-1}$$

where e/h is the intrinsic hadron to electromagnetic response ratio which is fited from the data together with the constants E_0 and m. Best fit parameters for stand-alone HE are $e/h = 1.216 \pm 0.005$, $m = 0.823 \pm 0.003$, and $E_0 = 1.24 \pm 0.17$ GeV. Figure 20 shows the dependence on beam momentum for stand alone HE and combined HE + EEP. More details about measurements of π/e at low energy with CMS HCAL may be found in Ref. [14].

Figure 21 shows the relative difference of the energy between all events and minimum ionizing pulses in EE from the forward part of HE. The solid line is a Monte Carlo calculation based on the longitudinal shower shape for different energies. For HE the longitudinal energy loss in EE is in the range 0.1 to 1% for pion energies from 30-300 GeV. This fraction is important for punch through of hadrons into the first layer of HE.

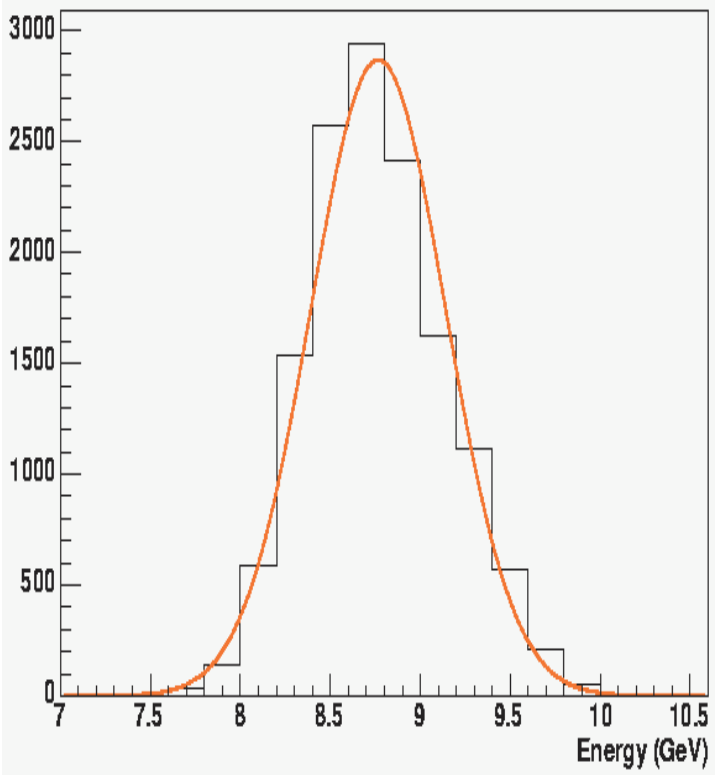

Figure 16: Energy distribution of pedestals (sum of five time 25 ns samples) for a HE single tower. The *rms* is $\sigma = 0.38$ GeV.

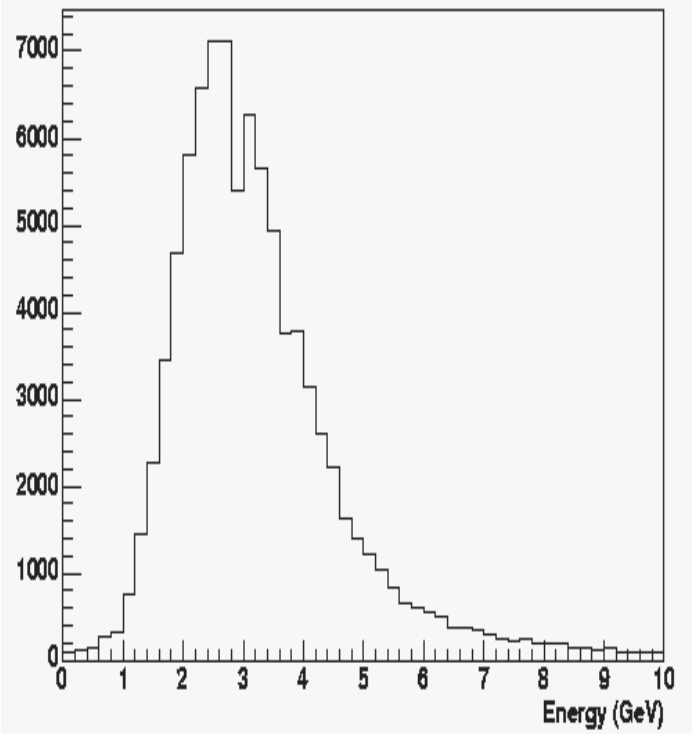

Figure 17: Energy distribution for 150 GeV muons where all HE layers in a single tower are summed.

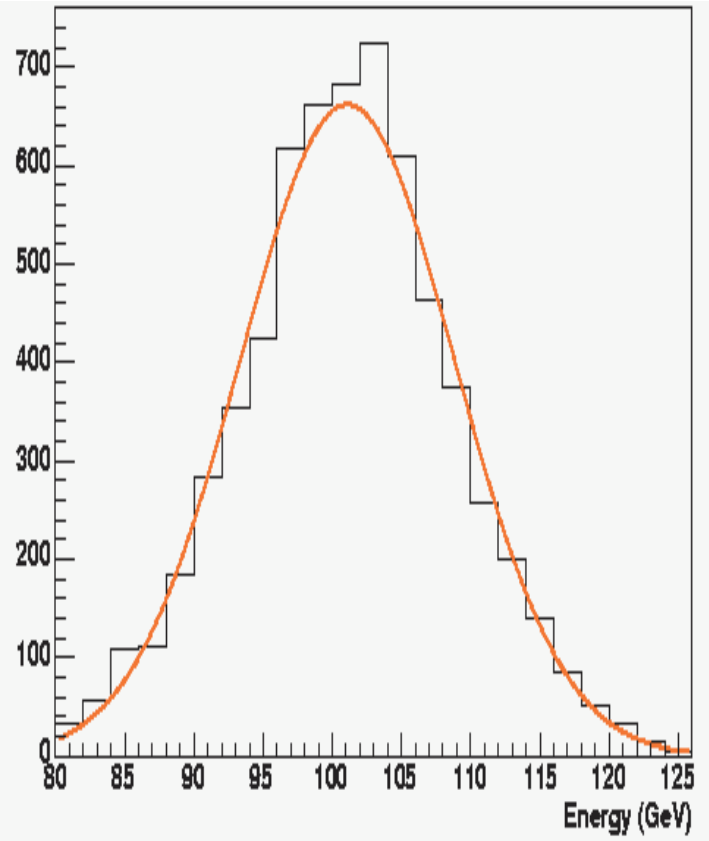

Figure 18: Energy distribution in HCAL for 100 GeV electrons. This data set the absolute HE calibration for this phase of data taking.

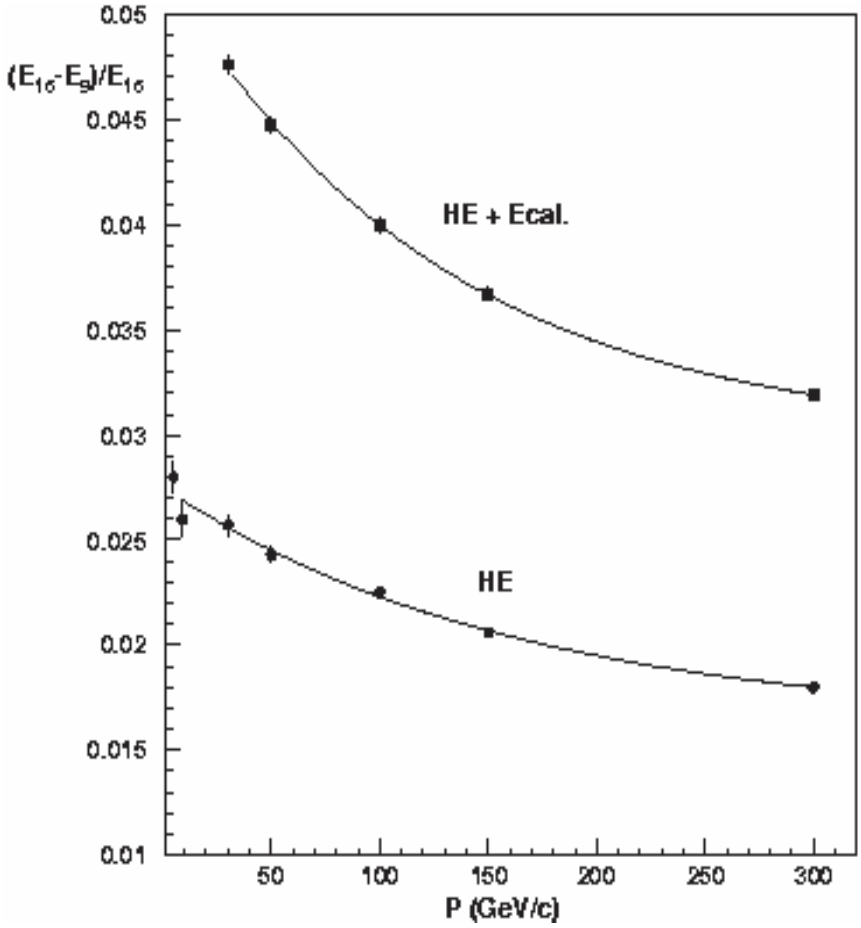

Figure 19: The ratio $(E_{16} - E_9)/E_{16}$ *vs.* beam momentum where the energy E_{16} is defined using 16 towers (18, 19, 20, and 21 $\times$ 4) and the energy E_9 is defined using 9 towers(19, 20, and 21 $\times$ 3). The signal difference was used to estimate the average transverse energy leakage.

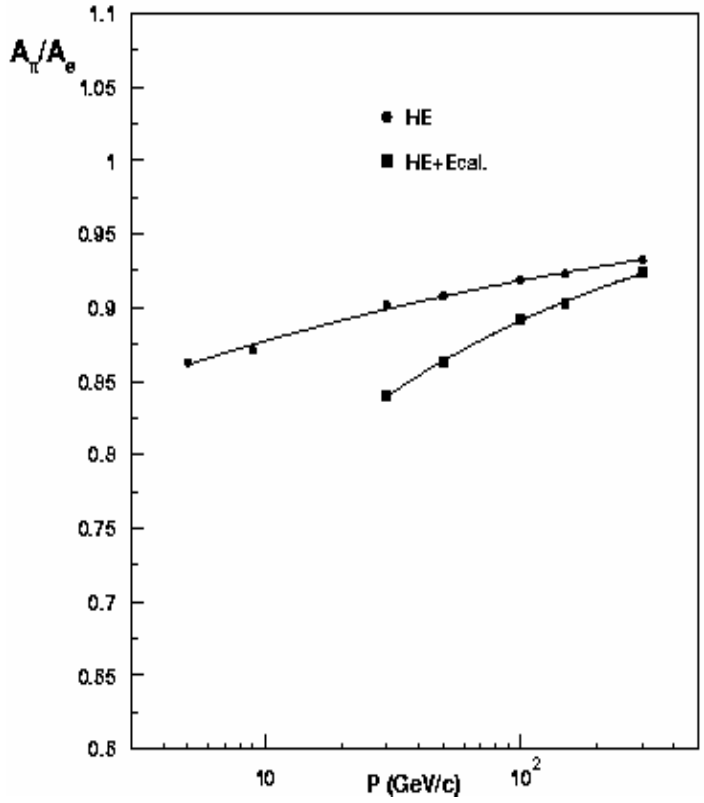

Figure 20: The π/e ratio for the hadron calorimeter with (squares) without EEP (circles).

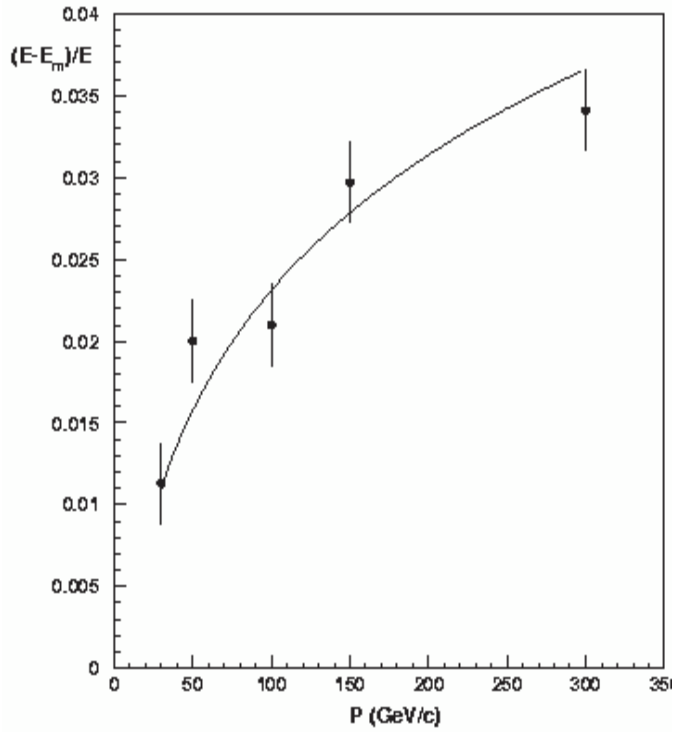

Figure 21: Ratio of total pion energy minus the minimum pion energy released before interacting in HCAL to the total pion energy as a function of pion beam momentum. The solid line is a Monte Carlo calculation using the longitudinal hadron shower distribution for different energies.

The energy resolution of the calorimeter is fit to the following expression:

$$\frac{\sigma}{E} = \frac{A}{\sqrt{E}} \oplus B \oplus \frac{\sigma_{\rm ped}}{E} \ ,$$

where A and B and constants and $\sigma_{\rm ped}$ is the measured contribution of the pedestal noise width to the resolution. The best fit parameters are: for pions in stand-alone HE (no EEP) $A = 1.061 \pm 0.004$ GeV$^{1/2}$, $B = 0.040 \pm 0.001$, for electrons in stand-alone HE (no EEP) $A = 0.670 \pm 0.004$ GeV$^{1/2}$, $B = 0.029 \pm 0.002$, and pions in HE+EEP $A = 1.188 \pm 0.006$ GeV$^{1/2}$, $B = 0.040 \pm 0.001$. Figure 22 shows the dependence of the fractional energy resolution for these three cases on the mean beam momentum. Note that these results for HE alone are consistent with those shown in Figure 14.

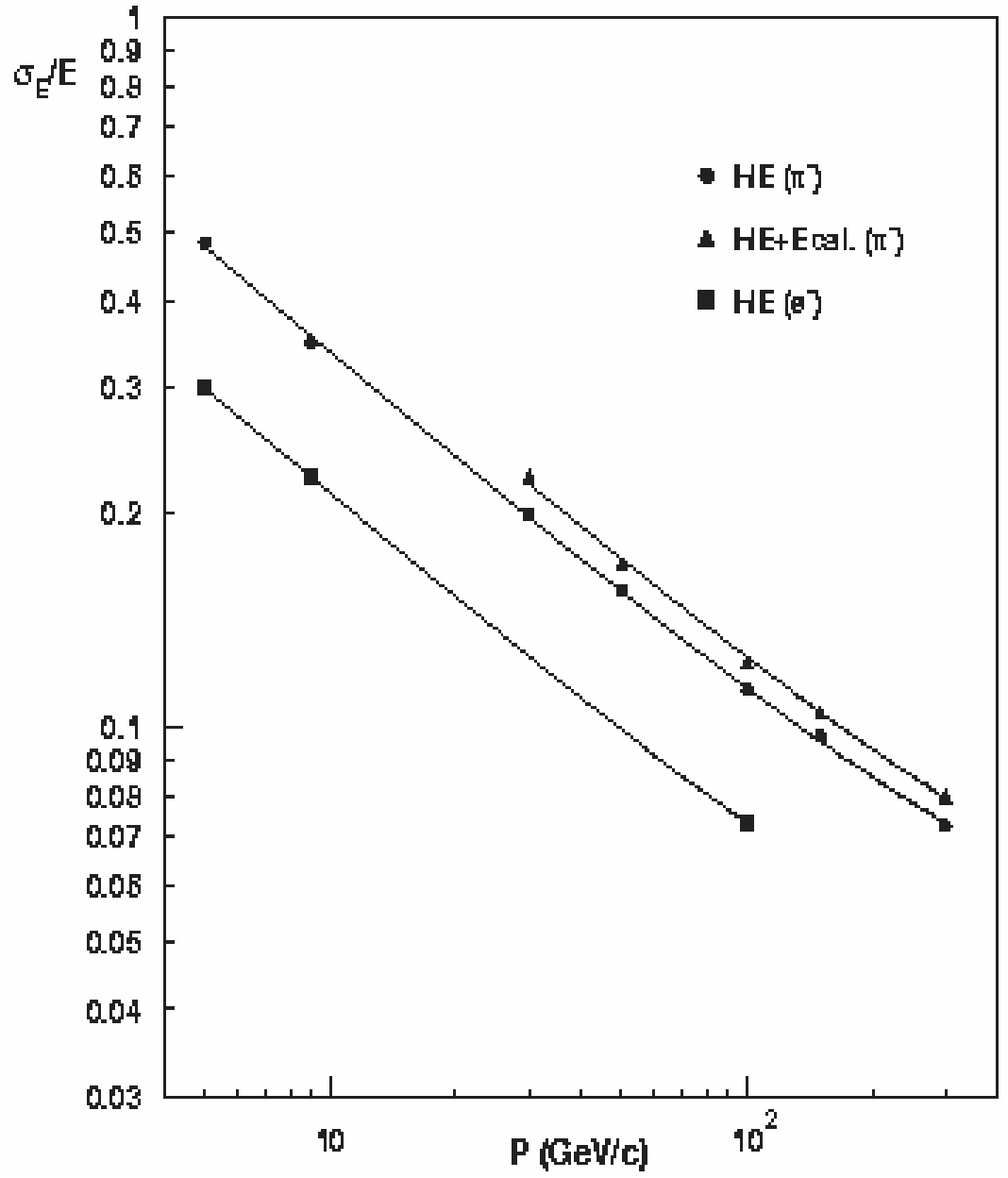

Figure 22: Calorimeter fractional energy resolution as a function of the beam momentum.

4.3 Spatial Resolution

The calorimeter can provide good position information. The spatial resolution of HE for pion showers was measured without ECAL in front of the HE prototype. Experimental data includes scans at pion energies of 50, 100, 200 and 300 GeV for the ϕ region from -2.5° to +2.5° degrees at fixed η (tower 19) as shown in Figure 23.

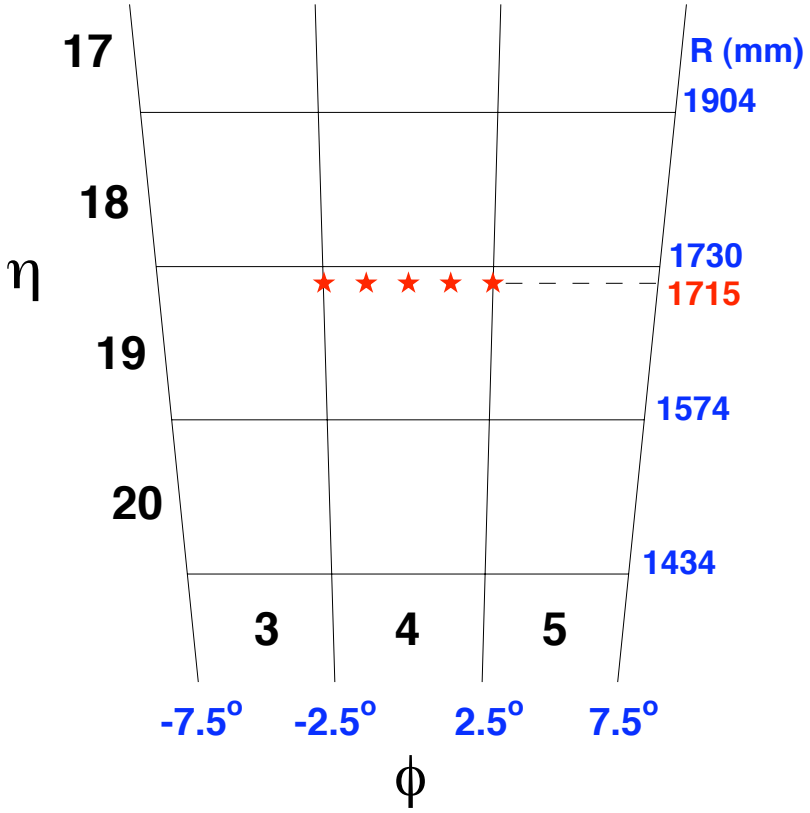

Figure 23: Schematic of the front part of the HE sector prototype, specifying the tower numbering in the η, ϕ directions, ϕ coordinates of the tower borders, and r coordinate in mm. Stars show the positions of the centers of the pion beam for 5 the exposures of the scan.

The ϕ position in degrees was measured by using the energy weighted center of gravity of the showers in 3×3 towers and was then compared with the position of the pion beam on the front face of HE measured by the beam chambers. Figure 24 shows the ϕ resolution *vs.* the ϕ coordinate of the pion beam at a momentum of 300 GeV/c. The best ϕ resolution corresponds to the pion position between the towers at $\phi = \pm 2.5°$ where the pion shower is equally shared between 2 towers and the worst case to the middle of a tower at $\phi = 0°$.

The dependence of the ϕ resolution on the beam momentum at fixed positions of the beam at $\phi = 0°, 1.25°$ and $2.5°$ is shown in Figure 25. The energy dependence of the ϕ resolution is described by the equation $\sigma = a \oplus b/\sqrt{E}$. The ϕ resolution ranges from 5% to 20% of the tower ϕ size for the different pion positions and energies used in this data set.

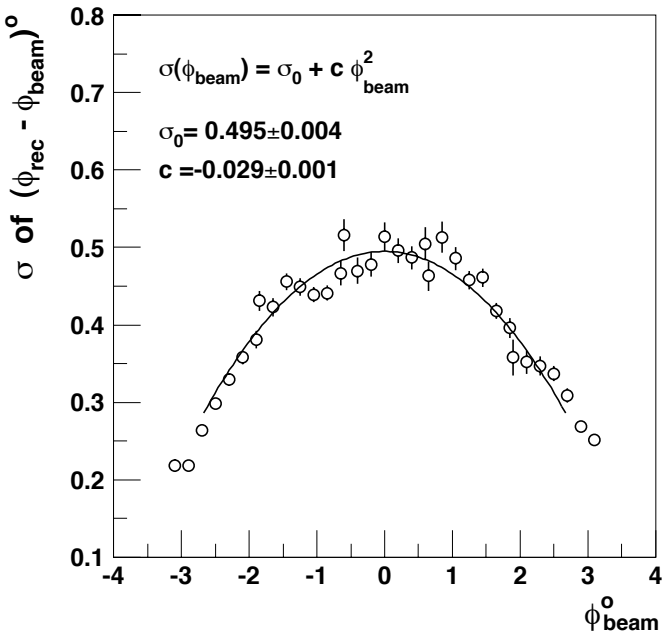

Figure 24: Resolution of HE in ϕ for pion showers as a function of the beam position for 300 GeV pions

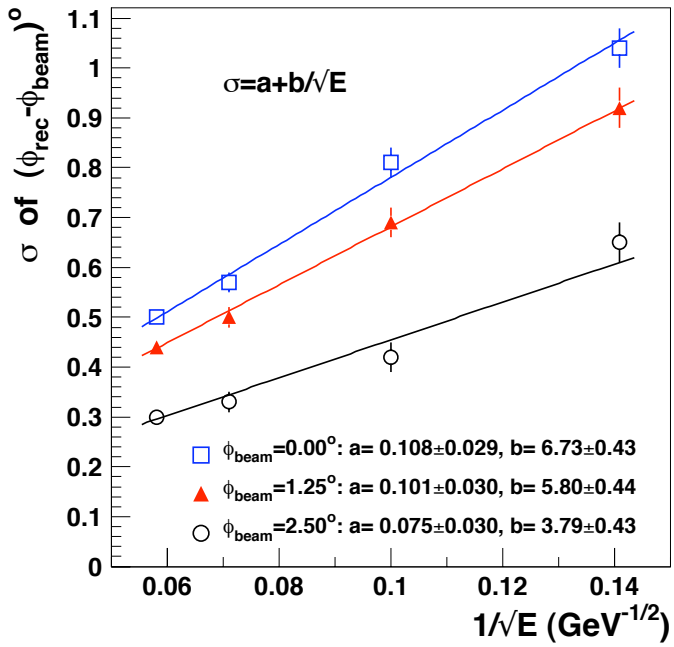

Figure 25: Resolution in ϕ for pion showers as a function of beam momentum,E_π , and best-fit curves for various positions of the pion beam.

5 Laser and LED System

The light system (Figure 26) consists of light emitting diodes (LEDs) and an ultraviolet nitrogen laser either of which can be switched on independently. The LED system illuminates the HPD directly and provides an absolute time signal for each channel. It is also used to give a fast qualitative check of the entire electronics chain. When the light system is switched to laser mode, the laser pulse passes through an attenuation filter rotor and a small portion of the light goes to a PIN diode (PIN 1) to monitor the intensity and timing of the laser. The other part of the pulse is fed to a green scintillator such that the green light illuminates each pixel of all HPDs. The pulse height of these distributions normalized to the PIN 1 diode pulse amplitude monitors the stability and performance of the electronics chain starting from the HPD. In an alternate mode, the laser light can be sent directly to the HE scintillator tiles.

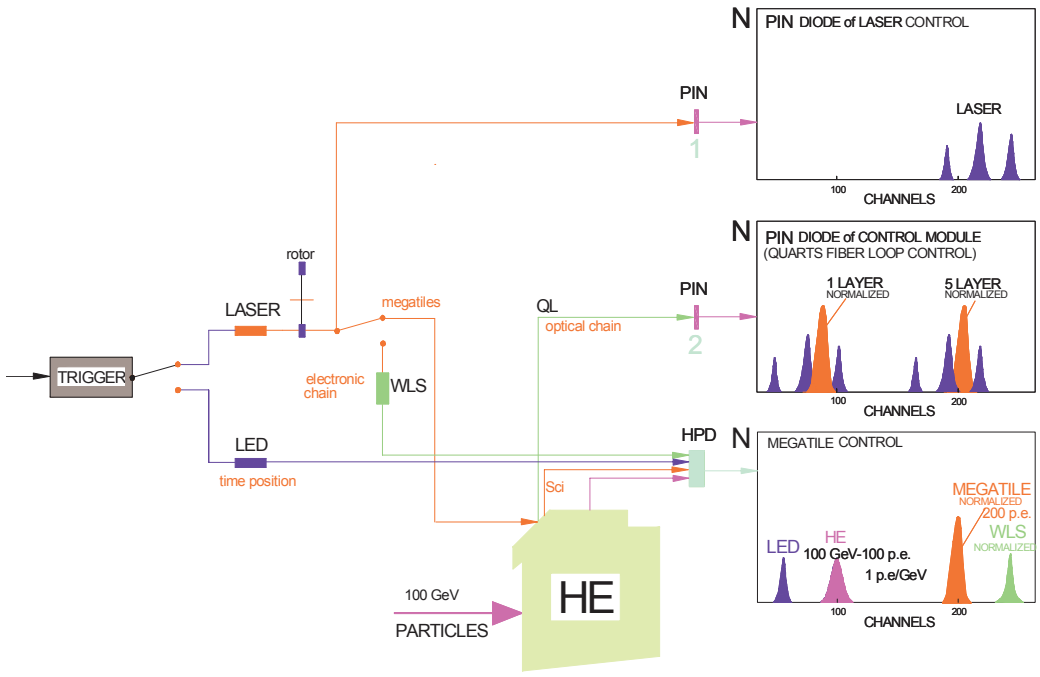

Figure 26: The layout of the optical control system.

Figure 9 shows (circles) the tiles which are illuminated by the laser. Light is transported to each scintillator tray by a quartz fiber where it is fanned out to 13 the independent tiles in the tray. The laser light is also sent to a WLS and then to a second PIN diode (PIN 2) to monitor the signal stability and the light transmission chain. The light to the tiles is used to monitor the radiation damage of the scintillators and the complete chain of performance of HE.

Figure 27 shows the HPD pulse height distribution from the WLS illuminated by laser (not normalized to PIN 1 diode). Figure 28 shows the same distribution normalized to the PIN 1 diode. Note the 2% width of this distribution. Figure 29 shows the pulse height distribution of a tile illuminated by the laser. Figure 30 shows the pulse height distribution from the PIN 2 diode.

A neutral density variable filter wheel was used to set the laser light intensity. These data are shown in Figure 31. The light intensity as measured by the HPD pulse height depends on the rotor position and in the range (100-7000) fC reproducible to better than 1%. Saturation starts at 10,000 fC due to the limited dynamic range of the front end electronics. However, more than 2 orders of magnitude of dynamic range can be monitored. Figure 32 shows the time distribution of HPD pulses in response to the laser. Time synchronization of the different HPD channels was done by setting front end electronics delays and using the fact that the laser light was simultaneous at the front face of all HPD by design [13]. Figure 33 shows the mean HPD pulse height values during the run. The pulse intensity uniformity of the laser system is 30 %.

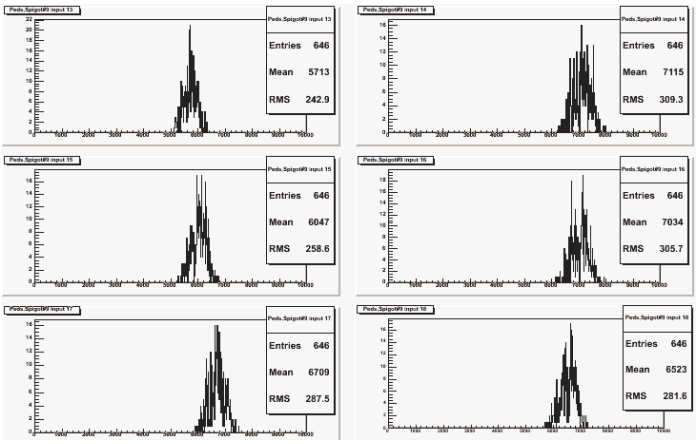

Figure 27: Pulse-heght distribution of the HPD illuminated by the laser.

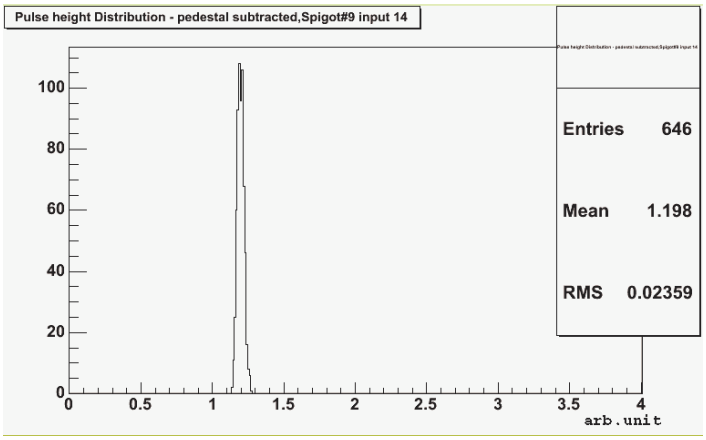

Figure 28: The HPD pulse-height distribution from LEP pulses normalized to the PIN-1 diode.

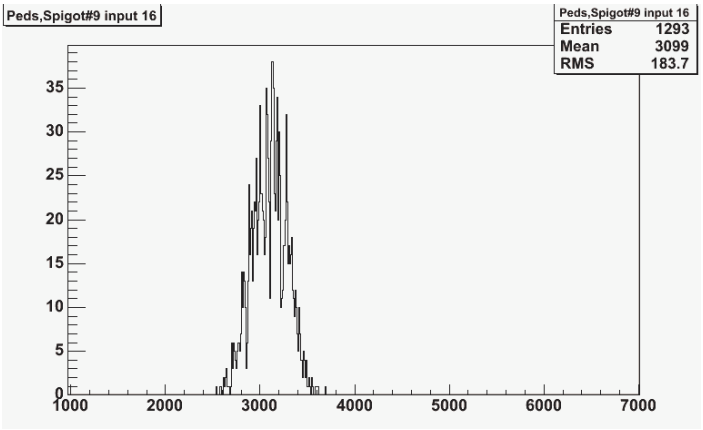

Figure 29: Pulse-height distribution from scintillator due to laser light injection into the tiles

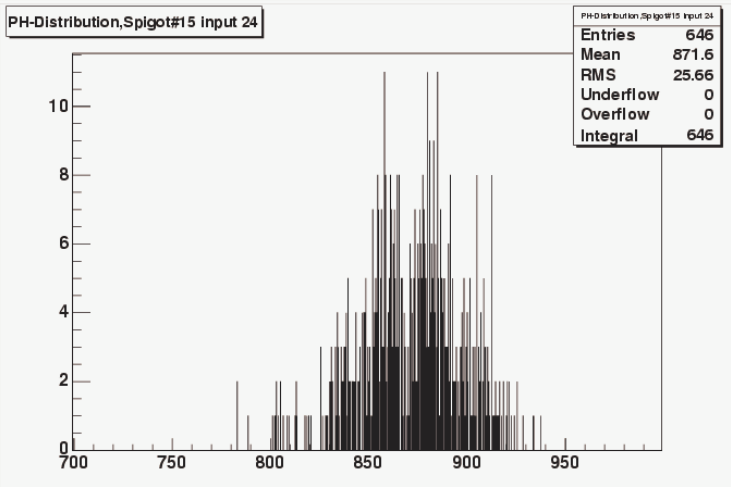

Figure 30: The PIN-2 diode signal from the quartz fiber.

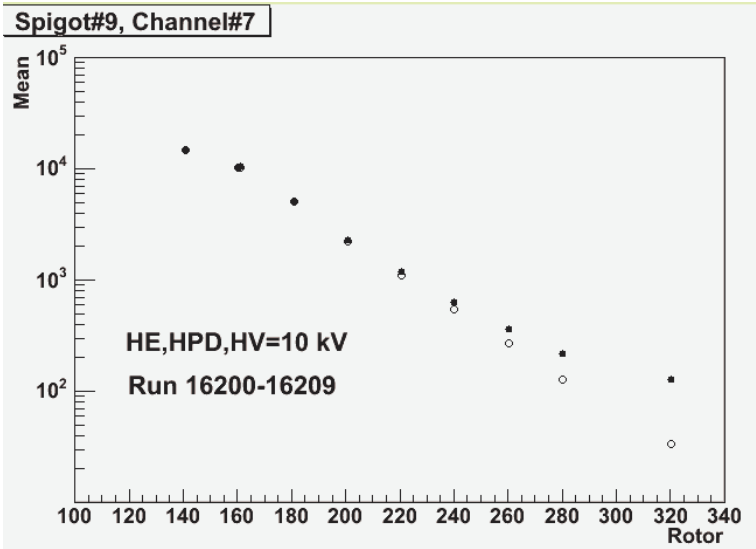

Figure 31: The HPD signals due to the laser light injectrion of a tile as a function of the filter rotor position before (closed circles) and after (open circles) pedestal subtraction.

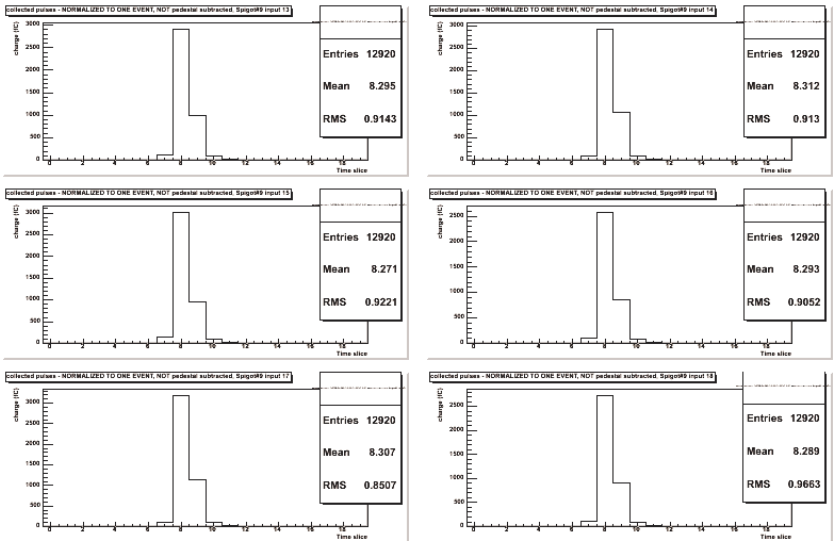

Figure 32: Time distribution of HPD pulses when a scintillator tile is excited by the laser after front end delays have been set. The time units are 25 ns, the time between successive bunch crossings at the LHC.

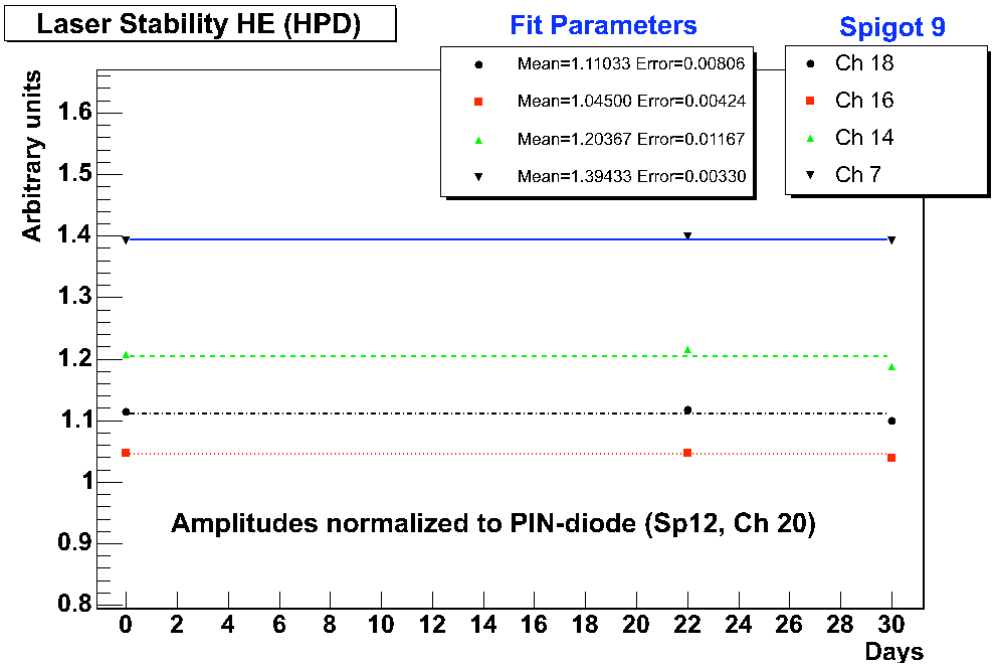

Figure 33: Mean HPD pulse height values due to excitation by laser light during the run.

6 Radioactive Source Calibration

Each tile of HE was exposed to a moving radioactive source in order to measure and monitor optical characteristics, and to transfer test beam calibrations with pions incident on the sector prototype (Figure 10) to the production HE calorimeter. Figure 34 shows the accumulated charge in a single tile as a function of the source position, both as the source is extended into the tile and then retracted. Figure 35 shows an enlargement of the region of peak signal averaged over source into the tile and retraction signals. The central half of the plateau was used to calculate a net (average) response for each tile.

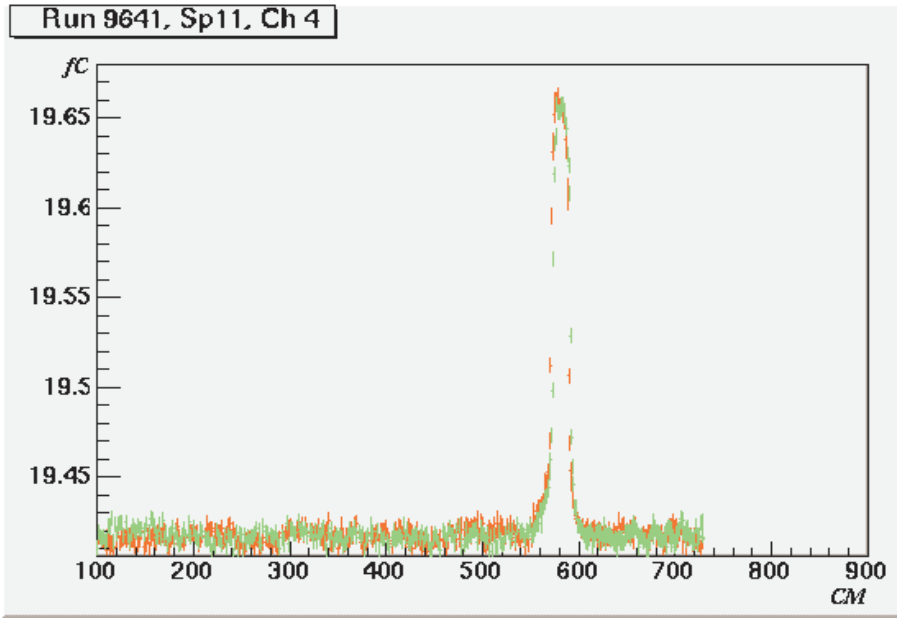

Figure 34: Radioactive source signal for one tile.

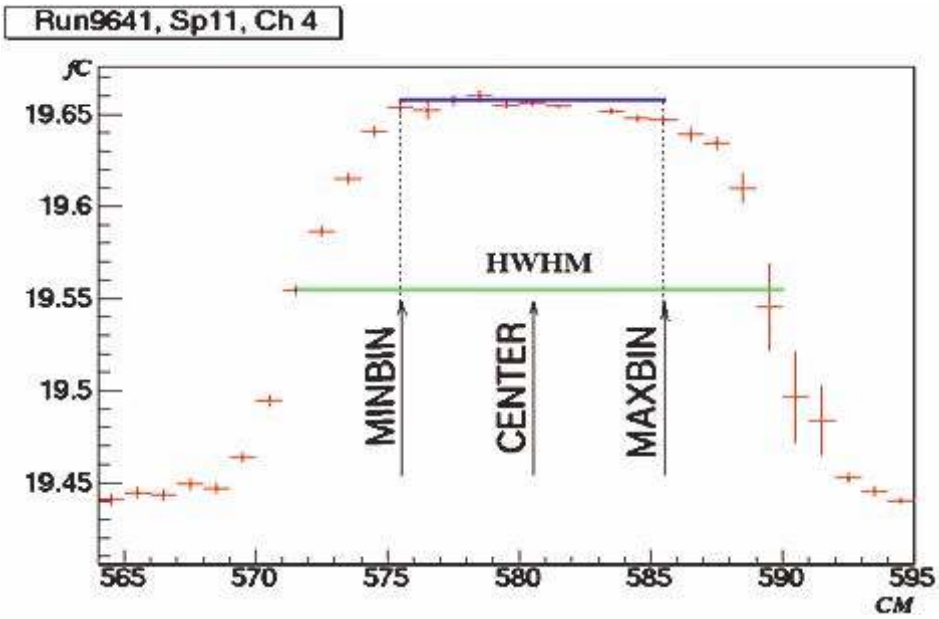

Figure 35: Calculation of the radioactive source tile signal by averaging over the center of the plateau.

The data from the set of tiles forming a HE tower were then combined to form source signals for both the front and rear longitudinal compartments of the towers. Figure 36 shows a comparison of the tower signals (front and rear plotted separately) as a function of both η and ϕ. The signals are normalized relative to the signal in the front part of of the tower corresponding to $\eta = 19, \phi = 4$. Because the radioactive wire source signal depends on

the tile dimensions, a correction was applied based on the relative signal obtained with a collimated radioactive source and the installed surface tubes and wire source at the time of scintillator assembly. The differences in source response values reflect the difference in optical paths length (attenuation) of the signals from tile to HPD. These data, compared with test beam pion data, are consistent to about 5 %. The initial calibration of HE towers in CMS is the ratio of the radioactive moving wire source value to that of the prototype, multiplied by the calibration constant of the prototype determined by the pion beam.

A comparison (ratio) of the signals observed from the radioactive wire source with those observed using a beam of muons, is shown in Figure 37. A correction (small) is made for the incident angle of the muon since the test beam is axial and the HE towers point to the CMS vertex. The source and muon data show agreement to better than 4%. This fact implies that the radioactive wire source is a reliable methode to obtain the initial HE calibration constants.

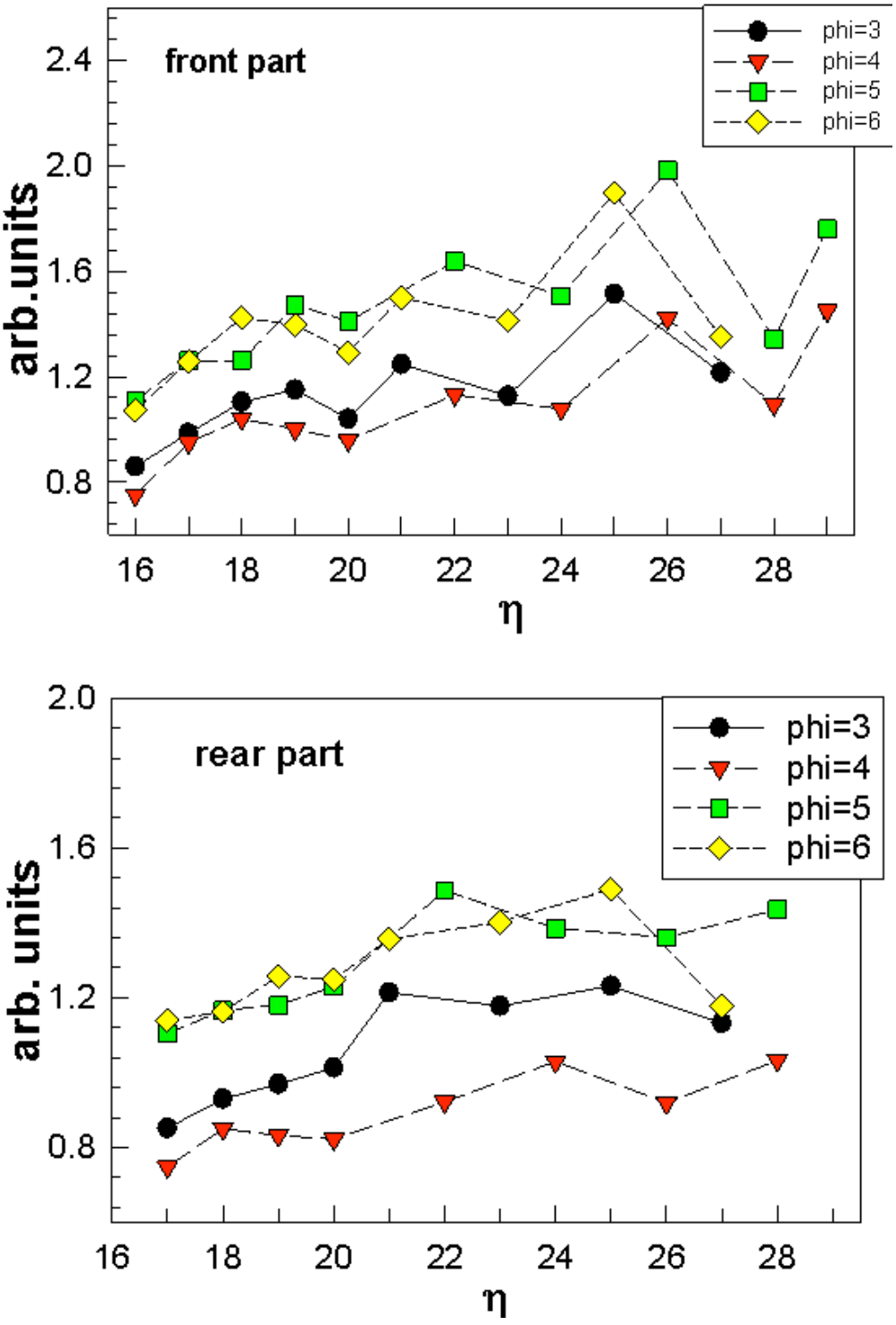

Figure 36: Radioactive source signals *vs.* tower number (η) for a) front and b) rear compartments. The signals are normalized relative to the signal in the front part of of the tower corresponding to $\eta = 19, \phi = 4$.

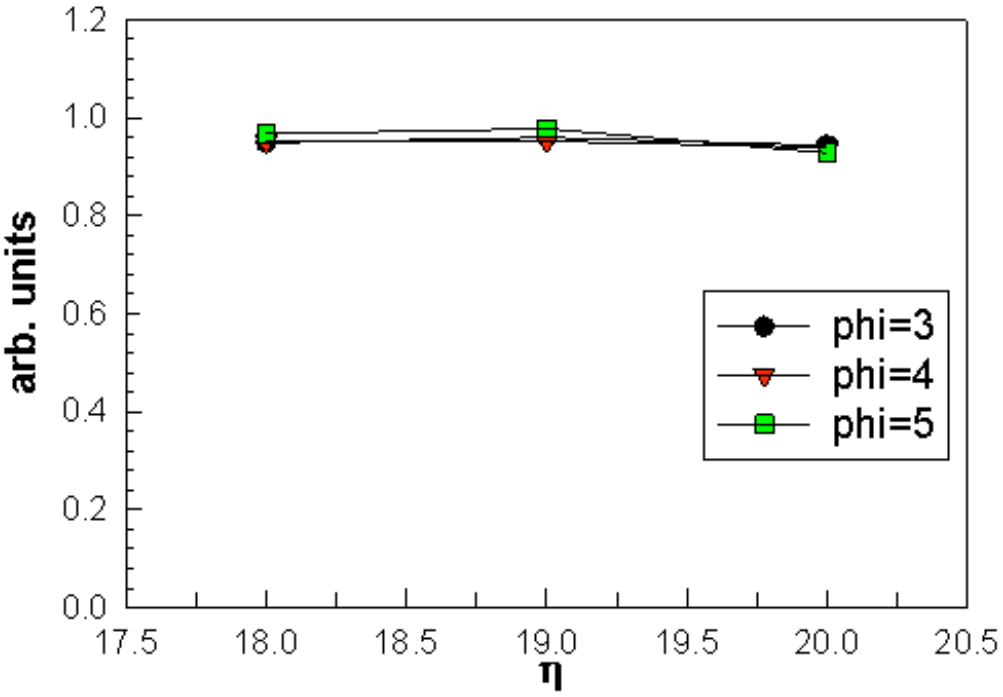

Figure 37: Ratio of radioactive source signal to muon beam signal for the rear part of HE towers.

7 Summary

1. The measured relationships between the initial energy deposited by the radioactive source, beam muons, and beam hadrons will define the energy scale calibration of the HE.

2. The pulse width from the hadron calorimeter is determined by the scintillator and the WLS flouresence time constants. The majority of the signal of the signal is in a single bunch crossing interval of 25 ns.

3. Using the signal from a scintillation tile layer placed at the front of HE (after EEP), the nonlinearity of the combined calorimeter is restored for single hadrons.

4. Introduction of low-Z material up to 40 g/cm^2 in front of the hadron calorimeter does not appreciably degrade the energy resolution.

5. Performance of the calorimeter with final photodetectors (HPDs) and CMS HCAL specific electronics shows no difference in comparison with standard commercially available electronics and phototubes.

6. The first test of the complete laser system was successful, as was the LED and radioactive wire source system.

Acknowledgments

We thank V. A. Polyakov for providing use of the electromagnetic calorimeter.

References

[1] "CMS Technical Proposal," CERN/LHCC 94-38, LHCC/P1 (December 1994).

[2] "CMS, The Hadron Calorimeter Technical Design Report," CERN/LHCC 97-31 CMS TDR 2 (June 1997).

[3] CMS HCAL Collaboration, "Design, Performance, and Calibration of CMS Hadron-Barrel Calorimeter Wedges,' CMS Note-2006/138, submitted to EPJ-C.

[4] A. Heister *et al.*, CMS Note 2006/036.

[5] H. Pi *et al.*, CMS Note 2006/035 (2006), EPJ-C in press.

[6] V. I. Kryshkin and A. I. Ronzhin, Nucl. Instr. Meth. **A 247** (1986) 583.

[7] M.G. Albrow *et al.*, Nucl. Instr. Meth. **A 256** (1987) 23.

[8] CMS HCAL Collaboration, CMS Note-2006/143.

[9] S. N. Malyukov *et al.*, JINR PI-95-283 (1995).

[10] D. Alde *et al.* Nucl. Inst. Meth. **A 268** (1988) 112; F. G. Binon *et al.* Nucl. Inst. Meth. **A 269** (1988) 101.

[11] T. Zimmerman and J. R. Hoff, IEEE J. Solid-State Circuits 39 (2004) 895.

[12] P. B. Cushman and A. H. Heering, IEEE Trans. Nucl. Sci. 49 (2002) 963.

[13] CMS HCAL Collaboration, CMS Note 2006/139.

[14] CMS HCAL Collaboration, CMS Note-2006/143.